To the Graduate Council:

I am submitting herewith a thesis written by Brian A. Maicke entitled "Compressible Flow in Slab Rocket Motors." I have examined the final electronic copy of this thesis for form and content and recommend that it be accepted in partial fulfillment of the requirements for the degree of Master of Sciences, with a major in Aerospace Engineering.

Joseph Majdalani

Joseph Majdalani, Major Professor

We have read this thesis
and recommend its acceptance:

Roy Schulz

Ken Kimble

Accepted for the Council:

Anne Mayhew

Vice Chancellor and Dean of
Graduate Studies

(Original signatures are on file with official student records.)

Compressible Flow in Slab Rocket Motors

A Thesis

Presented for the

Master of Science

Degree

The University of Tennessee, Knoxville

Brian A. Maicke

December 2006

Copyright © 2006 by Brian A. Maicke.

All rights reserved.

Acknowledgments

First I would like to thank my parents, Robert and Linda Maicke. Without their guidance, inspiration, and support, I would not be where I am today. Second, I thank my wife, Tiffany, for her support and motivation that started me on this path. I would like to thank my advisor, Dr. Majdalani for his suggestions regarding the preparation of this thesis and for his insight during the research that led to it. Dr. Schulz and Dr. Kimble also have my gratitude for their many comments that helped to improve the final work.

Abstract

In this thesis, the compressible flow inside a rectangular, porous channel is considered. A Rayleigh-Janzen perturbation is applied to the inviscid, steady, two-dimensional, isentropic flow equations. Closed form expressions are derived for the main properties of interest. The results of the study are verified via numerical simulation, with laminar and turbulent models, and with available experimental data. The critical point where the flow field reaches sonic conditions is determined analytically. Our analysis captures the steepening of the velocity profiles that has been reported in several studies using either computational or experimental methods. Explicit design criteria are presented to quantify the effects of compressibility in rockets and other two-dimensional injection-driven chambers. Compressibility effects on motor performance are quantified through the use of ballistics calculations to determine the performance of a motor.

Contents

1 Introduction **1**

1.1 The Evolution of the Cartesian Flow Model 2

1.1.1 Berman's Solution 2

1.1.2 Taylor's Solution 3

1.1.3 Aerospace Applications 4

1.2 Motivation for Compressible Studies 5

1.3 Classification of Compressible Methods 6

1.3.1 One-Dimensional Compressible Flows 8

1.3.2 Two-Dimensional Compressible Flows 8

2 Problem Definition **13**

2.1 Geometry 13

2.2 Derivation of the Governing Equations 14

2.2.1 Vorticity Equation 14

2.2.2 Vorticity Transport 15

2.2.3 Momentum Equation 16

2.2.4 Isentropic Relations 16

2.3 Boundary Conditions 17

2.4 Nondimensional Formulation 18

2.4.1 Nondimensional Governing Equations 18

2.4.2 Nondimensional Boundary Conditions 19

3 Perturbation Solution **21**

3.1 Perturbation Expansions 21

3.1.1 Vorticity Equation Perturbation Expansion 23

3.1.2 Vorticity Transport Equation Perturbation Expansion 23

3.1.3 Momentum Equation Perturbation Expansion 24

3.1.4 Isentropic Relation Perturbation Expansion 25

3.1.5 Boundary Condition Expansion 26

3.2 Leading Order Solution 28

3.2.1 Leading Order Vorticty Transport Solution 28

3.2.2 Leading Order Vorticity Solution 29

3.2.3 First Order Thermodynamic Variables 31

3.3 First Order Solution 32

3.3.1 First Order Vorticity Transport Solution 33

3.3.2 First Order Vorticity Solution 34

3.3.3 Second Order Thermodynamic Variables 39

4 Results and Discussion **41**

4.1 Critical Length Calculation 41

4.2 Computational Verification of the Analytical Solution 43

4.2.1 Thermodynamic Properties 44

4.2.2 Velocity Verification 45

4.3 Theoretical and Experimental Comparisons 45

4.3.1 Pressure Comparison 46

4.3.2 Velocity Comparison 47

4.4 Streamlines 49

4.5 Compressible Design Criterion 50

4.6 Internal Ballistics 52

4.6.1 Mass Flow Rate 52

4.6.2 Thrust Force 53
4.6.3 Specific Impulse 53
4.6.4 Characteristic Velocity 55
4.6.5 Thrust Coefficient 56

5 Conclusions **59**

Bibliography **61**

Appendix **67**

Vita **70**

List of Figures

2.1 Porous channel with an inert headwall. 14

4.1 Computational verification of the center-axis pressures and temperatures. . 45
4.2 Comparison of predicted center-axis velocity with numerical results. 46
4.3 Comparison of center-axis pressures to former studies. 47
4.4 Comparison of axial velocities at various motor locations. 48
4.5 Axial velocity comparison with Balakrishnan *et al.*. 49
4.6 The effects of compressibility on the streamlines of a slab rocket motor. . . 50
4.7 The specific impulse for a) $a_0 = 323$ m/s and b) $a_0 = 1500$ m/s. 55
4.8 Evolution of the characteristic velocity. 57
4.9 Thrust coefficient for increasing motor length. 58

Chapter 1

Introduction

Flow modeling has been a vital part of fluid mechanics since its inception. Often the governing equations required to define an engineering problem are so intricate that no analytical solution is readily available. Through flow modeling it is possible to consider a practical application and through judicious use of limiting assumptions and simplifications, arrive at a solution that captures the essence of the problem and approximates the behavior observed in experiments.

Fluid models also serve to further our understanding of specific aspects of fluid mechanics. In an introductory course to viscous fluid flow,[1] students beginning a study of viscosity do not start with flow over an airfoil, but rather with flow between a fixed and a moving plate. After this conceptual model is mastered, students graduate to more complex models such as the flow between axially moving or rotating cylinders. In this way, evolving flow models form the foundation of much of our understanding of fluid mechanics.

The development of flow models for practical problems follows the same evolution. First a basic model is developed. As that first study is understood, more complete models are built by relaxing assumptions and including effects previously neglected. As each successive model becomes more realistic, so will the solution in its ability to predict experimental results. This graduated increase in accuracy does not, however, come without cost. The equations describing the more complete systems become more complex, the cost of solving

them analytically or computationally increases, and the ability to extract physical meaning from the solution diminishes. For these reasons, it is important to balance the accuracy of a solution and its complexity.

The model of interest for this thesis is the steady, two-dimensional, inviscid, isentropic, compressible flow of a fluid through a rectangular channel with mass injection through its porous sidewalls. More specifically we are interested in the steady flow of a solid rocket motor in a long, two-dimensional configuration. It is the aim of this thesis to extend the present knowledge of this flow by accounting for the effects of compressibility on the parameters of interest.

1.1 The Evolution of the Cartesian Flow Model

Just as the fluid mechanics student examines flow over a flat plate before graduating to different models, understanding the first conceptual models for this type of channel may be useful before solving the compressible analog. There are many benefits to studying the previously published models. These allow the researcher to see past methods, which can help to guide the approach to new problems. They also give a sense of what limitations were faced in the past, and if it is possible to overcome them with newer technology or methods.

1.1.1 Berman's Solution

One of the first models detailing this type of fluid motion was put forth by Berman.[2] He found a steady, viscous, incompressible solution to the rectangular channel problem by constraining the normal velocity of the fluid to be independent of axial position. A stream function approach was employed to reduce the Navier-Stokes equations to the following nonlinear, third order, ordinary differential equation:

$$R(f'^2 - ff'') + f''' = k \tag{1.1}$$

Berman posits that when the injection velocity is small, the effects of the transverse flow through the porous walls can be determined by a perturbation expansion using a Reynolds number as a perturbation parameter. This insight comes from the fact that the solution to the viscous Cartesian channel flow without permeable walls is the well known Poiseuille flow described by

$$f''' = k \tag{1.2}$$

It is reasonable to conclude that the influence of the injection from the walls is a displacement effect on the flow, a result of the term that is multiplied by the Reynolds number in Eq. (1.1).

Berman's solution is for a case of uniform suction, but the results for an injection case are analogous. His solution is the first attempt to find the pressure field and velocity profile information for all points in the flow. Berman observes that the velocity profile with uniform suction is flatter than the traditional Poiseuille profile near the center-axis, while being steeper near the walls. He also notes that the total pressure drop for a given length of channel is higher when the walls are impermeable.

Berman's study is invaluable since it sets the standard for investigations of this nature. Not only is the study worthwhile as a mathematical exercise, but Berman translates the mathematical solution into understandable physical terms. It is not enough to simply state a solution to the equations of motion, it is necessary to interpret those results in physically significant ways to further improve our understanding of flows through porous membranes.

1.1.2 Taylor's Solution

The work of Sir Geoffrey Taylor[3] is another landmark study in the modeling of internal flow fields. Taylor examines the fluid flow in a wedge and in a cone with permeable walls. As in Berman's study, Taylor's primary concern is toward the effect of suction applied through the walls on the resulting flow field. Taylor also considers the limiting case as the angle of the wedge or cone goes to zero, defining the effects of suction flow in a slab or cylindrical

geometry. Taylor, like Berman, determines an incompressible, steady state solution to his problem. However, Taylor's solution differs from Berman's in that it is an inviscid solution.

In addition to extending the permeable wall solution to multiple configurations, Taylor uses a different method of solution. Rather than the differential approach of Berman, Taylor solves an integral form of the continuity equation. He does this by modeling the permeable walls as having resistance values which determine how easily the fluid could flow normal through the wall. When applied to the limiting cases of the parallel plane and the cylinder, Taylor finds that the axial velocity distribution is given by familiar cosine functions:

$$u\sqrt{\frac{\rho}{2S}} = \cos\frac{\pi y}{2b} \quad \text{for parallel planes} \tag{1.3}$$

$$u\sqrt{\frac{\rho}{2S}} = \cos\frac{\pi y^2}{2b^2} \quad \text{for cylinders} \tag{1.4}$$

where ρ is the density, S is the suction applied as determined by the resistance of the porous sheet with units of pressure (Pa), u is the longitudinal velocity, and b is the height of the chamber. It is also important to note that y varies from 0 to b. The establishment of the cosine profiles is not Taylor's only contribution to the permeable wall problem. He also conducts experiments with both porous cylinders and cones in which convincing verifications of the velocity profiles are presented. These experiments illustrate the validity of the normal injection approach for studying the permeable wall problem, and show that accurate predictions for this type of motion are possible.

1.1.3 Aerospace Applications

The first application of the permeable walled flow to rocketry is achieved by Culick.[4] Using a differential stream function approach to the axisymmetric problem, he is able to solve the vorticity equation in terms of the stream function. With an incompressible solution to the stream function, Culick is then able to determine the other parameters of interest, velocity, pressure distribution, etc. Culick's motivation for determining the mean flow in a cylindrical chamber is to further the understanding of the influence of the surface-injected mass flow

on the mean flow in the chamber and on the acoustic waves present in the simulated rocket motor.

Because Culick is the first to approach the problem from a rocketry standpoint, his study forms the basis of further investigations of channel flows in aerospace applications. Indeed, in this study we extend his incompressible stream function approach to account for the compressibility of the flow. It will be shown that the leading order approximation is Culick's incompressible solution for the two-dimensional flow case.

Because Culick shows that Taylor's analysis of the permeable walled channel gives a reliable approximation to the core flow inside a solid rocket motor, further study of the phenomenon is now possible. While Culick's solution is inviscid, the normal injection condition applied at the injection surface enables the fluid motion to retain critical features of the real, complex, reactive flow field. To this date, Culick's incompressible model remains one of the most cited and utilized models in solid rocket theory. It has been repeatedly considered by Traineau *et al.*,[5] Apte and Yang,[6] Najjar *et al.*,[7] Balakrishnan *et al.*,[8] Beddini and Roberts,[9] and many others. The justification for its ubiquitous use stems from two key factors: the apparent suitability of non-reactive models to simulate the harsh environment inside a real rocket motor and the validity of using a non-deformable permeable chamber with non-regressing walls. The first factor may be attributed to propellant heat release being confined to the relatively thin flame zone forming above the burning surface (Chu *et al.*[10]). The second factor may be associated with the weak sensitivity of the streamline curvature to the wall regression rate. As shown by Zhou and Majdalani[11] the effects of propellant regression are small in the operational range of most motors.

1.2 Motivation for Compressible Studies

The motivation for extending the solution to include compressibility has several reasons. While there have been studies that attempt to determine the effects of compressibility in solid rocket motors, none of these manage to capture the fully two-dimensional behavior

in a closed form analysis. The most notable of these previous studies are analyses by Traineau *et al.*,[5] King,[12] Flandro,[13] Balakrishnan *et al.*,[14] and Gany and Aharon.[15] Most are pseudo-one-dimensional or limited to numerical integral formulations; moreover, studies with analytical solutions often bear more severe limitations or restrictions than those imposed in the present work. Evidently, if a compressible analog to the Taylor-Culick profile can be found, then inviscid solutions would continue to be valuable to advance the theory of internal, rotational, compressible, and even reactive flow. Secondly, with increases in computational power and complexity in available solvers, more accurate and extensive analytical models become highly desirable to verify the efficacy of new computational methods. Just as an analytical solution by itself is of limited value without experimental or numerical confirmation, so do new computational codes require up-to-date analytical models for verification. Next, an improved compressible model can provide the foundation for more elaborate analysis. A compressible steady flow model can also help investigators to recast the time-dependent flow models for rocket motors; the existing relations can support the stationary and even traveling waves that are established in actual rocket motor operation, and which may be affected by compressibility effects (Majdalani[16]). Finally, a compressible Taylor representation could be applied to the nozzleless motor concept. As explained by Gany and Aharon,[15] the nozzleless motor gains in simplicity what it lacks in power. The removal of the nozzle does lower the efficiency of the motor, but the cost savings gained from eliminating what can be a complex nozzle assembly may make the nozzleless motor an attractive, low cost alternative in some (ramboosting) applications.

1.3 Classification of Compressible Methods

With the motivation for the study clearly defined, one must determine a solution methodology. Many different approaches have been used in compressible flow theory. Different approaches have different benefits and are applicable to certain sorts of problems. Flows can be classified in a number of ways. Internal flows are bounded or partially bounded by

walls that contain the flow field. The primary interest in this type of flow is the effects of the walls on the flow. External flows are concerned with a body surrounded by the flow field. However the most important factor in determining a solution method is the dimensionality of the motion. Most solutions are classified as either one-dimensional or multi-dimensional. Often, as long as the dimensionality of the solution is consistent, it can be applied to internal or external flows. As a result, we further examine the solution methods for one-dimensional and multi-dimensional flows.

There are many numerical methods that can be applied to compressible flow theory. For example, the method of characteristics, no longer in vogue, has been successfully applied to compressible flows, specifically to the design of supersonic nozzles.[17] This method is limited by the requirement that the entire flow is supersonic, which is not the case in the slab rocket motor. The relaxation method is another finite difference method that can capture both subsonic and supersonic mixed flows.[18] In solid rocket research, Traineau *et al.*[5] solve the equations numerically using a two-dimensional integration of the Euler equations via a finite volume predictor-corrector method to compare with their experimental and theoretical results. Vuillot and Avalon[19] solve the two-dimensional, laminar, compressible, unsteady Navier-Stokes equations to understand the effects of compressibility on the acoustic boundary layers in solid motors. More recently, Wasistho *et al.*[20] have conducted numerical simulations in an attempt to quantify the effects of compressibility on the transition to turbulent flow. Today, commercial CFD codes can be used to explore compressible flow problems with different solver methods. While these methods will generate a solution, they are not chosen as the primary method of analysis for this study because they do not provide closed form solutions. If no method is available to determine a closed form solution, then the numerical methods provide a necessary resource. Therefore, in the sections that follow we limit the discussion to analytical methods.

1.3.1 One-Dimensional Compressible Flows

One-dimensional flow is composed of flow in a single direction, with all derivatives perpendicular to the chosen direction vanishing. Taylor[21] demonstrates that this type of flow can be solved via closed form integration if the flow is adiabatic. A more general solution allowing for heat conduction is provided by von Mises.[22]

More limited solutions have also been determined. The most basic of these models being steady one-dimensional flow in a channel. Since the flow in such a channel is almost entirely axial, this assumption often gives a good approximation of the realistic compressible flow in such a configuration. Rayleigh and Fanno flows inside a channel are good examples of typical one-dimensional, compressible solutions.[23] For most channel flows, these solutions are good representations. However, for the rocket motor case the injection of mass perpendicular to the axial velocity makes the problem multi-dimensional and, as a result, more elaborate methods are required.

Most one-dimensional models do not require special techniques once limiting assumptions are applied. This is the reason that they are so popular for modeling not only truly one-dimensional flows, but also quasi-one-dimensional flows, where variations perpendicular to the streamwise velocity are negligible.

1.3.2 Two-Dimensional Compressible Flows

Since the flow for the slab motor is two-dimensional, one would expect that two-dimensional methods would yield the most promising avenues to address the problem. To that end, we present a survey of different two-dimensional methods and a brief summary of their advantages and disadvantages for handling the present problem.

The first solution method is that of the small perturbation theory. This method is most often applied to external flows over slender bodies. Since the disturbances caused by the body are small, one can use linearized equations to find an approximate solution to the flow field. A classical example of this method is flow over a wavy wall shown by Ackeret.[24] While the small perturbation theory works well for slender bodies subjected to external

flows or for internal flows with slightly tapered walls, it is not appropriate for the present study.

The hodograph method is another way to solve compressible flow problems.[25] Here one chooses the velocities as independent variables instead of the geometric coordinates normally used. The benefit of this transformation is that with the change in variable, the stream function becomes linear with respect to the velocity variables, and as a result becomes more susceptible to solution. The equations in the hodograph plane are often reducible using complex variable methods. Classic examples of hodograph theory include work by Tsien[26] and von Kármán[27] who were primarily interested in external flows over various body shapes. Cohen[28] more recently used the hodograph technique in the design of high-lift airfoils. The hodograph method can be a powerful method, but it also has limitations attached to it. In the literature it is primarily used for external flows. It is possible to adapt it to handle the internal flow in the present study, but the effort could be prohibitive. A more acute problem is that while transformation to the hodograph plane can facilitate a solution, it also makes translation back to the laboratory coordinates difficult. This makes comparisons to other work in the rocket motor field a cumbersome proposition as transformations back and forth between the hodograph and the laboratory coordinates would be required.

The next method for consideration is the Prandtl-Glauert expansion.[18] This method uses an expansion based on a shape parameter present in the flow field of interest. The velocities of interest are expanded in a series of the shape parameter. In this manner, one substitutes the expanded variables back into the equations and then segregates them by order of the shape parameter. These perturbed equations are then solved via traditional methods to determine the solution to the flow field. In a series of NACA reports, Kaplan[29–31] successfully applies the Prandtl-Glauert expansion to a number of different external flows.

In work more applicable to this study, a variation of this method was used by Balakrishnan *et al.*[14] to determine the flow field properties in a long, slender rocket motor. In this work, Balakrishnan and his coworkers expand the governing equations in terms of the

shape parameter h/a, where h is the height of the motor and a is the length. For long, slender motors this parameter is small thus reducing the truncation error in Balakrishnan's approximate pseudo-two-dimensional approach. Applying this expansion to the governing equations produces at the leading order,

$$\frac{\partial}{\partial x}\left(\rho u x^k\right) + \frac{\partial}{\partial y}\left(\rho v x^k\right) = 0 \tag{1.5}$$

$$\rho u \frac{\partial u}{\partial x} + \rho v \frac{\partial u}{\partial y} = -\frac{\partial p}{\partial x} \tag{1.6}$$

$$\frac{\partial p}{\partial y} = 0 \tag{1.7}$$

and

$$\rho u \frac{\partial}{\partial x}\left(c_p t + \tfrac{1}{2}u^2\right) + \rho v \frac{\partial}{\partial y}\left(c_p t + \tfrac{1}{2}u^2\right) = 0 \tag{1.8}$$

where u and v are the axial and transverse velocities, ρ is the density, p is the pressure, t is the temperature, c_p denotes the specific heat at constant pressure, and k is zero for two-dimensional flows and unity for the axisymmetric case. Note the approximation in the transverse momentum equation. This set is then transformed by introducing the stream function to produce the following

$$\sqrt{\frac{\gamma}{\gamma-1}} = \int_0^x \left(\frac{\Xi}{X}\right)^k \left[\frac{P(\Xi)}{P(X)}\right]^{\frac{1}{\gamma}} \left\{1 - \left[\frac{P(X)}{P(\Xi)}\right]^{(\gamma-1)/\gamma}\right\}^{-1/2} d\Xi \tag{1.9}$$

where Ξ is a nondimensional strained coordinate in the axial direction and γ is the ratio of specific heats. Equation (1.9) is then integrated numerically to determine the pressure distribution with respect to X. With the pressure distribution determined, the other physical properties can be determined by substitution back into the governing equations.

The Prandtl-Glauert expansion method is a valid method to use for the present study but there are two concerns that arise from employing it. The first concern is that the solution is limited to long, slender motors since the perturbation expansion requires the shape parameter to be small. For shorter motors it is possible that this method will deteriorate.

The second concern is that the resulting equations from the shape expansion must be numerically integrated to produce a solution. To find a closed-form solution, another method must be employed.

The final method presented here is the Rayleigh-Janzen perturbation expansion. So named after the work presented by Janzen[32] and Rayleigh[33] in solving compressible flows, the Rayleigh-Janzen method requires one to expand the variables in a series of the Mach number squared. In this manner, one substitutes the expanded variables back into the equations and then segregates them by order of the Mach number. These perturbed equations can then be solved by traditional methods to determine the solution to the flow field. Unlike the small perturbation linearization, the Rayleigh-Janzen method is suited for both external flows and internal flows.

This technique is used by Flandro[13] in the context of a compressible, internal burning, solid rocket motor. However, Flandro uses the expansion to solve quasi-one-dimensional forms of the governing equations; his solution is limited by its inability to satisfy the compressible, first order, vorticity transport equation. More recently, the Rayleigh-Janzen expansion has been applied successfully by Majdalani[34] to determine the compressible analog to the Taylor-Culick flow field in a cylindrical geometry. While the Rayleigh-Janzen method has been used to analyze other flow fields, notably the work on Hill's spherical vortex by Moore and Pullin[35] and the Stuart vortex by Mieron *et al.*,[36] it has not been widely applied to multi-dimensional fluid motions, leaving open the possibility of using this approach in other previously untreated internal flow problems.

Unlike the Prandtl-Glauert expansion, this method is not restricted by the size of the motor, making it ideal for handling a wide range of aspect ratios. It does require that the characteristic wall Mach number used in the expansion process to be small; for the range of rocket motor operation a small wall Mach number is virtually assured. As a result, the Rayleigh-Janzen method can render solutions that are valid over the entire range of motor aspect ratios and operating conditions. For these reasons, it is chosen as the primary method of analysis.

What follows is our analysis of the compressible slab rocket motor. In Chapter 2 the geometric model is defined and the limiting assumptions are introduced. Furthermore, the governing equations for the flow field are derived and non-dimensionalized. Chapter 3 introduces the Rayleigh-Janzen perturbation expansion and illustrates the solution methodology. The results of the study are presented in Chapter 4, complete with comparisons to previous models and numerical and experimental verifications. Design criteria and performance characteristics are also derived. Chapter 5 brings the study to its conclusion, summarizing the results and discussing possible extensions and continuations based on this work.

Chapter 2

Problem Definition

2.1 Geometry

To model the semi-infinite two-dimensional rocket motor flow field, i.e. the slab rocket motor, a rectangular chamber of length L_0 and half height of a is used. L_s is the sonic length and is specified as the distance from the origin that fluid in the chamber must travel to reach sonic conditions. The origin of the coordinate system describing the domain is located on the vertical center of the headwall. The spatial variables $\bar{x}$ and $\bar{y}$ are defined as the directions parallel and normal to the center-axis. The motor extends to infinity in the $\bar{z}$-axis direction. Taking advantage of symmetry, a solution can be obtained for the top half of the geometry, namely $0 \leq \bar{y} \leq a$ and $0 \leq \bar{x} \leq L_0$, and mirrored across the center-axis. Figure 2.1 depicts the solution domain for the slab motor.

Along the solid, porous sidewalls of the rocket, a uniform injection velocity of U_w is imposed. While there are any number of factors that could affect the local velocity at the propellant surface, density fluctuations, localized non-homogeneity of the propellant, and erosive burning, to name a few, this constraint gives a reasonable approximation of the injection mechanism at the propellant surface. The headwall of the motor is solid and inert, giving a zero axial velocity boundary condition at the headwall.

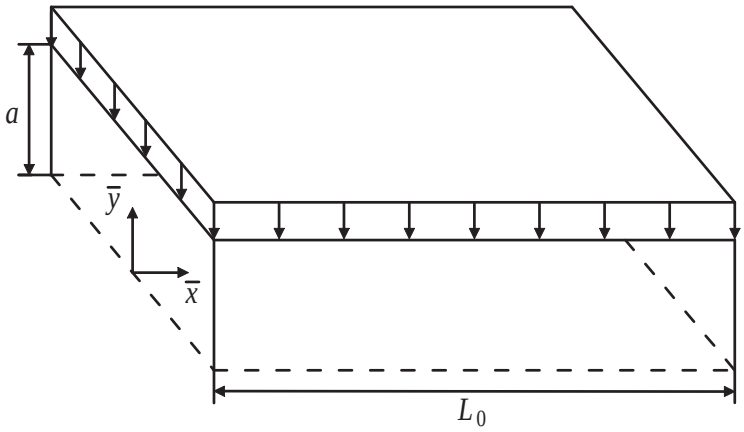


Figure 2.1: Porous channel with an inert headwall.

2.2 Derivation of the Governing Equations

A stream function approach is at the heart of the solution covered in this thesis. To facilitate this approach, the following expressions relating the velocities and the stream function are used. These are

$$\bar{u} = \frac{1}{\bar{\rho}} \frac{\partial \bar{\psi}}{\partial \bar{y}} \tag{2.1}$$

$$\bar{v} = -\frac{1}{\bar{\rho}} \frac{\partial \bar{\psi}}{\partial \bar{x}} \tag{2.2}$$

where the over-bar indicates dimensional variables.

2.2.1 Vorticity Equation

The vorticity equation is used to derive the main sets of governing equations in perturbation variables for the flow. Recalling the definition of vorticity for two-dimensional Cartesian flow, one has

$$\bar{\mathbf{\Omega}} = \bar{\nabla} \times \bar{\mathbf{U}} = \left(\frac{\partial \bar{v}}{\partial \bar{x}} - \frac{\partial \bar{u}}{\partial \bar{y}} \right) \hat{k} \tag{2.3}$$

where $\bar{\mathbf{U}} = u\hat{i} + v\hat{j}$. The stream function relations from Eqs. (2.1) and (2.2) are substituted into Eq. (2.3) and expanded to give the following scalar equation

$$\bar{\Omega} = -\frac{1}{\bar{\rho}}\left(\frac{\partial^2\bar{\psi}}{\partial\bar{x}^2} + \frac{\partial^2\bar{\psi}}{\partial\bar{y}^2}\right) - \frac{\partial\bar{\psi}}{\partial\bar{x}}\frac{\partial}{\partial\bar{x}}\left(\frac{1}{\bar{\rho}}\right) - \frac{\partial\bar{\psi}}{\partial\bar{y}}\frac{\partial}{\partial\bar{y}}\left(\frac{1}{\bar{\rho}}\right) \tag{2.4}$$

Evaluating the derivative terms containing density produces

$$\bar{\Omega} = -\frac{1}{\bar{\rho}}\left(\frac{\partial^2\bar{\psi}}{\partial\bar{x}^2} + \frac{\partial^2\bar{\psi}}{\partial\bar{y}^2}\right) + \frac{1}{\bar{\rho}^2}\frac{\partial\bar{\psi}}{\partial\bar{x}}\frac{\partial\bar{\rho}}{\partial\bar{x}} + \frac{1}{\bar{\rho}^2}\frac{\partial\bar{\psi}}{\partial\bar{y}}\frac{\partial\bar{\rho}}{\partial\bar{y}} \tag{2.5}$$

Equation (2.5) is multiplied by $-\bar{\rho}$, to isolate the stream function. The scalar equation is further simplified by rewriting the last two terms using vector notation,

$$\frac{\partial^2\bar{\psi}}{\partial\bar{x}^2} + \frac{\partial^2\bar{\psi}}{\partial\bar{y}^2} = \frac{1}{\bar{\rho}}\left(\bar{\nabla}\bar{\rho}\cdot\bar{\nabla}\bar{\psi}\right) - \bar{\Omega}\bar{\rho} \tag{2.6}$$

Equation (2.6) is the coupled vorticity stream function equation used in this study.

2.2.2 Vorticity Transport

In order to solve Eq. (2.6), another equation relating vorticity and the stream function is required. After some manipulation, the momentum equation provides the necessary form. First, the general inviscid momentum equation is

$$\bar{\rho}\frac{D\bar{\mathbf{U}}}{D\bar{t}} = \bar{\rho}\bar{\mathbf{f}} - \bar{\nabla}\bar{p} \tag{2.7}$$

Expanding the substantial derivative in Eq. (2.7) results in

$$\bar{\rho}\left(\frac{\partial\bar{\mathbf{U}}}{\partial\bar{t}} + \bar{\nabla}\frac{\bar{\mathbf{U}}\cdot\bar{\mathbf{U}}}{2} - \bar{\mathbf{U}}\times\bar{\nabla}\times\bar{\mathbf{U}}\right) = \bar{\rho}\bar{\mathbf{f}} - \bar{\nabla}\bar{p} \tag{2.8}$$

Since the problem is defined as a steady flow problem, the time dependent term is dropped from Eq. (2.8). Body forces are also neglected in the present study, so Eq. (2.8) can be

further simplified by removing $\bar{\rho}\bar{\mathbf{f}}$. One has

$$\bar{\rho}\left(\bar{\nabla}\frac{\bar{\mathbf{U}}\cdot\bar{\mathbf{U}}}{2}-\bar{\mathbf{U}}\times\bar{\nabla}\times\bar{\mathbf{U}}\right)=-\bar{\nabla}\bar{p} \tag{2.9}$$

In order to find the necessary relation between vorticity and stream function, it is expeditious to first divide by $\bar{\rho}$ and then take the curl of both sides of Eq. (2.9). At the outset, one gets

$$\bar{\nabla}\times\left(\bar{\mathbf{U}}\times\bar{\mathbf{\Omega}}\right)=\frac{1}{\bar{\rho}^2}\bar{\nabla}\bar{\rho}\times\bar{\nabla}\bar{p} \tag{2.10}$$

Equation (2.10) is the general, three-dimensional vorticity transport equation which provides the additional needed relationship between vorticity and stream function.

2.2.3 Momentum Equation

In order to determine the pressure in the chamber, the vector momentum equation is worked into a more tractable form. Relating the pressure to the stream function, Eq. (2.9) becomes

$$\bar{\rho}\bar{\nabla}\left\{\frac{1}{2\bar{\rho}^2}\left[\left(\frac{\partial\bar{\psi}}{\partial\bar{y}}\right)^2+\left(\frac{\partial\bar{\psi}}{\partial\bar{x}}\right)^2\right]\right\}+\bar{\rho}\left(+\frac{1}{\bar{\rho}}\frac{\partial\bar{\psi}}{\partial x}\bar{\Omega}\hat{i}+\frac{1}{\bar{\rho}}\frac{\partial\bar{\psi}}{\partial y}\bar{\Omega}\hat{j}\right)=-\bar{\nabla}\bar{p} \tag{2.11}$$

after Eqs. (2.1) and (2.2) are substituted. Simplifying the equation and rewriting it in the more compact, vector notation yields

$$\bar{\rho}\bar{\nabla}\left[\frac{1}{2\bar{\rho}^2}\left(\bar{\nabla}\bar{\psi}\cdot\bar{\nabla}\bar{\psi}\right)\right]+\bar{\Omega}\bar{\nabla}\bar{\psi}=-\bar{\nabla}\bar{p} \tag{2.12}$$

2.2.4 Isentropic Relations

To formulate a complete solution to this problem, more relations are needed to bring closure to the thermodynamic properties. Pursuant to the assumptions and constraints of the model, we can use the non-dimensional isentropic flow equations of a calorically perfect gas:

$$\rho=p^{\frac{1}{\gamma}} \tag{2.13}$$

and

$$T = p^{\frac{\gamma-1}{\gamma}} \tag{2.14}$$

2.3 Boundary Conditions

With the problem domain established and the governing equations defined, it is important to have a full understanding of the boundary conditions. Mathematically, the boundary conditions are expressed as

$$\bar{v}(\bar{x}, 0) = 0 \tag{2.15}$$

$$\bar{u}(\bar{x}, a) = 0 \tag{2.16}$$

$$\bar{v}(\bar{x}, a) = -U_w \tag{2.17}$$

and

$$\bar{u}(0, \bar{y}) = 0 \tag{2.18}$$

Physically, Eq. (2.15) is a condition of symmetry. This constraint restricts flow from going across the center-plane of the chamber. Equation (2.16) represents no axial slip velocity and Eq. (2.17) establishes the wall blowing velocity. The first condition is normally reserved for viscous flows, but it is applied here successfully to ensure normal injection. The second condition sets the uniform injection velocity specified at the sidewalls of the chamber, to simulate the ejection of burning solid propellant gases. Finally, an inert headwall condition is imposed using Eq. (2.18).

2.4 Nondimensional Formulation

To facilitate the analysis, it is prudent to non-dimensionalize the variables of interest. A standard methodology is employed, resulting in the following parameters:

$$x = \frac{\bar{x}}{a}; y = \frac{\bar{y}}{a}; u = \frac{\bar{u}}{a_0}; v = \frac{\bar{v}}{a_0}; p = \frac{\bar{p}}{p_0}; T = \frac{\bar{T}}{T_0}; \rho = \frac{\bar{\rho}}{\rho_0}; \psi = \frac{\bar{\psi}}{a_0 \rho_0 a}; \Omega = \frac{\bar{\Omega} a}{a_0}; \nabla = a\bar{\nabla} \tag{2.19}$$

These relations can be substituted back into the governing equations and boundary conditions to generalize the problem for all solution domains, rather than just one specific case.

2.4.1 Nondimensional Governing Equations

Substitution of the nondimensional variables defined in Eq. (2.19) into Eq. (2.6) produces a vorticity equation containing dimensionless variables with coefficients of dimensional parameters:

$$\frac{a_0 \rho_0}{a}\left(\frac{\partial^2 \psi}{\partial x^2} + \frac{\partial^2 \psi}{\partial y^2}\right) = \frac{a_0 \rho_0}{a}\frac{1}{\rho}\left(\nabla \rho \cdot \nabla \psi\right) - \frac{a_0 \rho_0}{a}\Omega \rho \tag{2.20}$$

Since each term in the equation has the same collection of dimensional parameters, it is possible to divide through by the parameter to simplify the nondimensional vorticity equation to

$$\frac{\partial^2 \psi}{\partial x^2} + \frac{\partial^2 \psi}{\partial y^2} = \frac{1}{\rho}\left(\nabla \rho \cdot \nabla \psi\right) - \Omega \rho \tag{2.21}$$

A similar substitution can be made to Eq. (2.10). One gets

$$\frac{a_0^2}{a^2}\left[\nabla \times (\mathbf{U} \times \mathbf{\Omega})\right] = \frac{p_0}{\rho_0 a^2}\left(\frac{1}{\rho^2}\nabla \rho \times \nabla p\right) \tag{2.22}$$

This result can be simplified by multiplying both sides of the equation by a^2. Equation (2.22) is further reduced by realizing that $p_0/\rho_0 = a_0^2/\gamma$ from the definition of the speed of

sound in an ideal gas. The resulting simplified equation becomes

$$\nabla \times (\mathbf{U} \times \mathbf{\Omega}) = \frac{1}{\gamma \rho^2} \nabla \rho \times \nabla p \tag{2.23}$$

The momentum equation simplifies via the same procedure that produced Eq. (2.23). Substitution of the nondimensional relations defined in Eq. (2.19) into Eq. (2.12) yields

$$\frac{a_0^2 \rho_0}{a} \left\{ \rho \nabla \left[\frac{1}{2\rho^2} (\nabla \psi \cdot \nabla \psi) \right] + \Omega \nabla \psi \right\} = \frac{p_0}{a} (-\nabla p) \tag{2.24}$$

Equation (2.24) is simplified in the same manner as Eq. (2.22), namely by multiplying both sides by a and applying the definition of the speed of sound in an ideal gas. The result of this simplifcation is the finalized momentum equation.

$$\rho \nabla \left[\frac{1}{2\rho^2} (\nabla \psi \cdot \nabla \psi) \right] + \Omega \nabla \psi = -\frac{\nabla p}{\gamma} \tag{2.25}$$

The already non-dimensionalized isentropic relations in Eqs. (2.13) and (2.14) are not repeated here.

2.4.2 Nondimensional Boundary Conditions

In order to solve the simplified equations from Section 2.4.1, the boundary conditions also must have the same methodology applied to them. Using the non-dimensionalization scheme given by Eq. (2.19), the boundary conditions set forth in Eqs. (2.15)-(2.18) become

$$v(x, 0) = 0 \tag{2.26}$$

$$u(x, 1) = 0 \tag{2.27}$$

$$v(x, 1) = -M_w \tag{2.28}$$

and

$$u(0, y) = 0 \tag{2.29}$$

where M_w is the Mach number of the injected flow through the sidewall. With both the governing equations and the boundary conditions in the more general, non-dimensional form, the equations are ready to be solved.

Chapter 3

Perturbation Solution

In order to solve the set of governing equations, a Rayleigh-Janzen perturbation is applied. This requires the expansion of the primary flow variables in truncated series representations as follows:

$$\begin{aligned} u(x,y) &= M_w u_0 + M_w^3 u_1 + O(M_w^5) \quad & \rho(x,y) &= 1 + M_w^2 \rho_1 + M_w^4 \rho_2 + O(M_w^6) \\ v(x,y) &= M_w v_0 + M_w^3 v_1 + O(M_w^5) \quad & p(x,y) &= 1 + M_w^2 p_1 + M_w^4 p_2 + O(M_w^6) \\ \psi(x,y) &= M_w \psi_0 + M_w^3 \psi_1 + O(M_w^5) \quad & T(x,y) &= 1 + M_w^2 T_1 + M_w^4 T_2 + O(M_w^6) \\ \Omega(x,y) &= M_w \Omega_0 + M_w^3 \Omega_1 + O(M_w^5) \end{aligned} \tag{3.1}$$

The perturbation expansions of Eq. (3.1) are substituted back into the governing equations and then sorted by order of magnitude via standard perturbation methods.

3.1 Perturbation Expansions

Since the solution is in terms of the stream function, Eqs. (2.1) and (2.2) are used to relate the velocity components to ψ. Substitution of the appropriate perturbation expansions from Eq. (3.1) produces

$$M_w u_0 + M_w^3 u_1 = \frac{1}{1 + M_w^2 \rho_1 + M_w^4 \rho_2} \left(M_w \frac{\partial \psi_0}{\partial y} + M_w^3 \frac{\partial \psi_1}{\partial y} \right) \tag{3.2}$$

Then the following expansion is used to elevate the density terms from the denominator to the numerator viz.

$$(1 + X)^{-\alpha} = 1 - \alpha X + O\left(X^2\right) \tag{3.3}$$

Only the first two terms are kept to be consistent with the order of the perturbation solution. Substitution of Eq. (3.3) back into Eq. (3.2) gives

$$M_w u_0 + M_w^3 u_1 = \left(1 - M_w^2 \rho_1 - M_w^4 \rho_1\right) \left(M_w \frac{\partial \psi_0}{\partial y} + M_w^3 \frac{\partial \psi_1}{\partial y} \right) \tag{3.4}$$

Multiplying out the right hand side returns

$$M_w u_0 + M_w^3 u_1 = M_w \frac{\partial \psi_0}{\partial y} + M_w^3 \frac{\partial \psi_1}{\partial y} - M_w^3 \rho_1 \frac{\partial \psi_0}{\partial y} + O(M_w^5) \tag{3.5}$$

The equations are segregated by the order of M_w to give the leading and first order velocities and stream functions:

$$O(M_w) : u_0 = \frac{\partial \psi_0}{\partial y} \tag{3.6}$$

and

$$O(M_w^3) : u_1 = \frac{\partial \psi_1}{\partial y} - \rho_1 \frac{\partial \psi_0}{\partial y} \tag{3.7}$$

The same approach can be applied to the crossflow velocity v to yield:

$$O(M_w) : v_0 = -\frac{\partial \psi_0}{\partial x} \tag{3.8}$$

and

$$O(M_w^3) : v_1 = \rho_1 \frac{\partial \psi_0}{\partial x} - \frac{\partial \psi_1}{\partial x} \tag{3.9}$$

3.1.1 Vorticity Equation Perturbation Expansion

Equation (2.21) is subjected to the same set of perturbation variables defined in Eq. (3.1). One obtains

$$\begin{aligned} M_w\frac{\partial^2\psi_0}{\partial y^2}+M_w^3\frac{\partial^2\psi_1}{\partial y^2}+M_w\frac{\partial^2\psi_0}{\partial x^2}+M_w^3\frac{\partial^2\psi_1}{\partial x^2}= \\ \frac{1}{1+M_w^2\rho_1+M_w^4\rho_2}\left(M_w^2\nabla\rho_1+M_w^4\nabla\rho_2\right)\cdot\left(M_w\nabla\psi_0+M_w^3\nabla\psi_1\right) \\ -\left(M_w\Omega_0+M_w^3\Omega_1\right)\left(1+M_w^2\rho_1+M_w^4\rho_2\right) \end{aligned} \tag{3.10}$$

The series expansion in Eq. (3.3) is again used to eliminate the density terms in the denominator. The resulting equation is multiplied out and truncated to $O(M_w^5)$ to get

$$\begin{aligned} M_w\frac{\partial^2\psi_0}{\partial y^2}+M_w^3\frac{\partial^2\psi_1}{\partial y^2}+M_w\frac{\partial^2\psi_0}{\partial x^2}+M_w^3\frac{\partial^2\psi_1}{\partial x^2}= \\ M_w^3\left(\nabla\rho_1\cdot\nabla\psi_0\right)-M_w\Omega_0-M_w^3\left(\Omega_0\rho_1-\Omega_1\right) \end{aligned} \tag{3.11}$$

The terms of (3.11) are sorted by the wall Mach number such that

$$O(M_w):\frac{\partial^2\psi_0}{\partial y^2}+\frac{\partial^2\psi_0}{\partial x^2}=-\Omega_0 \tag{3.12}$$

and

$$O(M_w^3):\frac{\partial^2\psi_1}{\partial y^2}+\frac{\partial^2\psi_1}{\partial x^2}=\nabla\rho_1\cdot\nabla\psi_0-\Omega_0\rho_1-\Omega_1 \tag{3.13}$$

3.1.2 Vorticity Transport Equation Perturbation Expansion

Solving the leading order vorticity equation requires Eq. (2.23) to be subjected to the same perturbation treatment. After substitution of Eq. (3.1), the vorticity transport equation becomes

$$\begin{aligned} \nabla\times\left[\left(M_w\mathbf{U}_0+M_w^3\mathbf{U}_1\right)\times\left(M_w\boldsymbol{\Omega}_0+M_w^3\boldsymbol{\Omega}_1\right)\right]= \\ \frac{1}{\gamma\left(1+M_w^2\rho_1+M_w^4\rho_2\right)^2}\left[\nabla\left(1+M_w^2\rho_1+M_w^4\rho_2\right)\times\nabla\left(1+M_w^2p_1+M_w^4p_2\right)\right] \end{aligned} \tag{3.14}$$

Using the approximation from Eq. (3.3) allows one to expand Eq. (3.14) into

$$M_w^2 \left[\nabla \times (\mathbf{U}_0 \times \mathbf{\Omega}_0)\right] + M_w^4 \left[\nabla \times (\mathbf{U}_0 \times \mathbf{\Omega}_1) + \nabla \times (\mathbf{U}_1 \times \mathbf{\Omega}_0)\right] = M_w^4 \left(\nabla \rho_1 \times \nabla p_1\right) + O(M_w^6) \tag{3.15}$$

Which upon segregation leads to the following two equations for vorticity transport

$$O(M_w^2) : \nabla \times (\mathbf{U}_0 \times \mathbf{\Omega}_0) = 0 \tag{3.16}$$

and

$$O(M_w^4) : \nabla \times (\mathbf{U}_0 \times \mathbf{\Omega}_1) + \nabla \times (\mathbf{U}_1 \times \mathbf{\Omega}_0) = \nabla \rho_1 \times \nabla p_1 \tag{3.17}$$

3.1.3 Momentum Equation Perturbation Expansion

The momentum equation determines the pressure distribution throughout the chamber and as such, it is subjected to the same expansion process by introducing the terms in Eq. (3.1). After the substitutions are made, Eq. (2.25) becomes

$$\begin{aligned} -\frac{\nabla\left(1 + M_w^2 p_1 + M_w^4 p_2\right)}{\gamma} &= \left(1 + M_w^2 \rho_1 + M_w^4 \rho_2\right) \\ &\cdot \nabla \left\{ \frac{1}{2\left(1 + M_w^2 \rho_1 + M_w^4 \rho_2\right)^2} \left[\nabla\left(M_w \psi_0 + M_w^3 \psi_1\right) \cdot \nabla\left(M_w \psi_0 + M_w^3 \psi_1\right)\right] \right\} \\ &+ \left(M_w \Omega_0 + M_w^3 \Omega_1\right) \nabla\left(M_w \psi_0 + M_w^3 \psi_1\right) \end{aligned} \tag{3.18}$$

Next Eq. (3.3) is used to simplify the density terms by elevating them to the numerator. The resulting equation is multiplied out to yield

$$\begin{aligned} -\frac{M_w^2 \nabla p_1 + M_w^4 \nabla p_2}{\gamma} = & \\ & M_w^2 \left\{ \nabla \left[\frac{1}{2} \left(\nabla \psi_0 \cdot \nabla \psi_0\right) \right] - \Omega_0 \nabla \psi_0 \right\} \\ & + M_w^4 \left\{ \nabla \left[\left(\nabla \psi_0 \cdot \nabla \psi_1\right) - \rho_1 \left(\nabla \psi_0 \cdot \nabla \psi_0\right) \right] + \rho_1 \nabla \left(\frac{\nabla \psi_0 \cdot \nabla \psi_0}{2} \right) \right\} \\ & + M_w^4 \left(\Omega_0 \nabla \psi_1 + \Omega_1 \nabla \psi_0\right) \end{aligned} \tag{3.19}$$

The result is then arranged into relationships for the first and second order pressure terms:

$$O(M_w^2) : -\frac{\nabla p_1}{\gamma} = \nabla\left(\frac{\nabla\psi_0 \cdot \nabla\psi_0}{2}\right) + \Omega_0 \nabla\psi_0 \tag{3.20}$$

and

$$\begin{aligned} O(M_w^4) : -\frac{\nabla p_2}{\gamma} &= \nabla\left[(\nabla\psi_0 \cdot \nabla\psi_1) - \rho_1\left(\nabla\psi_0 \cdot \nabla\psi_0\right)\right] \\ &+\rho_1 \nabla\left(\frac{\nabla\psi_0 \cdot \nabla\psi_0}{2}\right) + \Omega_0 \nabla\psi_1 + \Omega_1 \nabla\psi_0 \end{aligned} \tag{3.21}$$

3.1.4 Isentropic Relation Perturbation Expansion

To bring closure to the solution, the isentropic relations in Eqs. (2.13) and (2.14) are perturbed using the Rayleigh-Janzen expansions from Eq. (3.1). One finds

$$1 + M_w^2\rho_1 + M_w^4\rho_2 = \left(1 + M_w^2 p_1 + M_w^4 p_2\right)^{\frac{1}{\gamma}} \tag{3.22}$$

Again expanding the right hand side, Eq. (3.22) becomes

$$1 + M_w^2\rho_1 + M_w^4\rho_2 = 1 + \frac{1}{\gamma}\left(M_w^2 p_1 + M_w^4 p_2\right) + \frac{(1/\gamma - 1)}{2\gamma} M_w^4 p_1^2 + O(M_w^6) \tag{3.23}$$

Segregating the equations by order up to $O\left(M_w^4\right)$ provides the two equations

$$O(M_w^2) : \rho_1 = \frac{p_1}{\gamma} \tag{3.24}$$

and

$$O(M_w^4) : \rho_2 = \frac{p_2}{\gamma} + \frac{1-\gamma}{2\gamma^2} p_1^2 \tag{3.25}$$

The temperature equation follows the same procedure, starting with the substitution of

$$1 + M_w^2 T_1 + M_w^4 T_2 = \left(1 + M_w^2 p_1 + M_w^4 p_2\right)^{\frac{\gamma-1}{\gamma}} \tag{3.26}$$

Following the same expansion procedure as before yields

$$1 + M_w^2 T_1 + M_w^4 T_2 = 1 + \frac{\gamma - 1}{\gamma}\left(1 + M_w^2 p_1 + M_w^4 p_2\right) + \frac{1 - \gamma}{2\gamma^2} M_w^4 p_1^2 + O(M_w^6) \tag{3.27}$$

This equation is then separated by order to provide the first and second order temperature terms:

$$O(M_w^2) : T_1 = \frac{\gamma - 1}{\gamma} p_1 \tag{3.28}$$

and

$$O(M_w^4) : T_2 = \frac{\gamma - 1}{\gamma} p_2 + \frac{1 - \gamma}{2\gamma^2} p_1^2 \tag{3.29}$$

3.1.5 Boundary Condition Expansion

The final step in the perturbation expansion process is to ensure the boundary conditions are consistent with the perturbation variables of the solution. As expected with normal perturbation expansions, the leading order boundary conditions resulting from the expansion become

$$v_0(x, 0) = 0 \tag{3.30}$$

$$u_0(x, 1) = 0 \tag{3.31}$$

$$v_0(x, 1) = -1 \tag{3.32}$$

and

$$u_0(0, y) = 0 \tag{3.33}$$

First, since the governing equation is written in terms of the stream function, it is convenient to rewrite these leading order boundary conditions in terms of the stream function

$$\frac{\partial \psi_0(x, 0)}{\partial x} = 0 \tag{3.34}$$

$$\frac{\partial \psi_0(x, 1)}{\partial y} = 0 \tag{3.35}$$

$$\frac{\partial \psi_0(x,1)}{\partial x} = 1 \tag{3.36}$$

and

$$\frac{\partial \psi_0(0,y)}{\partial y} = 0 \tag{3.37}$$

Second, since the boundary conditions must be satisfied by the leading order terms for the solution to be valid, the set of boundary conditions used to determine the higher order approximations must be homogeneous. For illustration, the first order homogeneous boundary conditions are shown here:

$$v_1(x,0) = 0 \tag{3.38}$$

$$u_1(x,1) = 0 \tag{3.39}$$

$$v_1(x,1) = 0 \tag{3.40}$$

and

$$u_1(0,y) = 0 \tag{3.41}$$

Equations (3.7) and (3.9) are then substituted into the boundary conditions to give the finalized boundary conditions for the first order approximation:

$$\rho_1 \frac{\partial \psi_0(x,0)}{\partial x} - \frac{\partial \psi_1(x,0)}{\partial x} = 0 \tag{3.42}$$

$$\frac{\partial \psi_1(x,1)}{\partial y} - \rho_1 \frac{\partial \psi_0(x,1)}{\partial y} = 0 \tag{3.43}$$

$$\rho_1 \frac{\partial \psi_0(x,1)}{\partial x} - \frac{\partial \psi_1(x,1)}{\partial x} = 0 \tag{3.44}$$

and

$$\frac{\partial \psi_1(0,y)}{\partial y} - \rho_1 \frac{\partial \psi_0(0,y)}{\partial y} = 0 \tag{3.45}$$

3.2 Leading Order Solution

The solution methodology that is adapted to the present problem is carried out as follows: First, solve the leading order vorticity equation for the stream function. After the leading order stream function is known, substitute it into the first order momentum and isentropic relations to determine the rest of the variables of interest. However, to solve Eq. (3.12), a relationship between vorticity and the stream function must first be determined. To that end, Eq. (3.16) is examined to provide such a relation.

3.2.1 Leading Order Vorticty Transport Solution

Equation (3.16) is expanded from its more compact vector notation in 2-D cartesian coordinates, using the definition of the cross product and curl operations to obtain

$$\frac{\partial}{\partial x}\left(u_0\Omega_0\right) + \frac{\partial}{\partial y}\left(v_0\Omega_0\right) = 0 \tag{3.46}$$

To find a relationship between the stream function and the vorticity, Eqs. (3.6) and (3.8) are substituted to get

$$\frac{\partial}{\partial x}\left(\frac{\partial\psi_0}{\partial y}\Omega_0\right) + \frac{\partial}{\partial y}\left(-\frac{\partial\psi_0}{\partial x}\Omega_0\right) = 0 \tag{3.47}$$

Properly evaluating the derivatives leads to a scalar equation for the vorticity component in the $\hat{k}$ direction, specifically,

$$\frac{\partial\psi_0}{\partial y}\frac{\partial\Omega_0}{\partial x} + \Omega_0\frac{\partial^2\psi_0}{\partial x\partial y} - \frac{\partial\psi_0}{\partial x}\frac{\partial\Omega_0}{\partial y} - \Omega_0\frac{\partial^2\psi_0}{\partial x\partial y} = 0 \tag{3.48}$$

and so

$$\frac{\partial\psi_0}{\partial y}\frac{\partial\Omega_0}{\partial x} = \frac{\partial\psi_0}{\partial x}\frac{\partial\Omega_0}{\partial y} \tag{3.49}$$

Equation (3.49) is satisfied when

$$\Omega_0 = F(\psi_0) \tag{3.50}$$

where F is any continuous function of ψ_0 with a first order analytic derivative. One such solution that is commonly used in the analysis of rocket motors is

$$\Omega_0 = C^2 \psi_0 \tag{3.51}$$

where C^2 is an appropriate constant whose value must be obtained in the course of the solution.

3.2.2 Leading Order Vorticity Solution

With Eq. (3.51) providing the necessary link between vorticity and the stream function, Eq. (3.12) is solved for the stream function. The stream function is then used to determine the leading order quantities of all parameters of interest. It is interesting to note that because the Rayleigh-Janzen expansion is used, the leading order part recovers the incompressible solution to the slab rocket motor. With this in mind, Eq. (3.51) is substituted into Eq. (3.12) such that

$$\frac{\partial^2 \psi_0}{\partial y^2} + \frac{\partial^2 \psi_0}{\partial x^2} + C^2 \psi_0 = 0 \tag{3.52}$$

This equation is easily separable assuming that

$$\psi_0 = f(x) g(y) \tag{3.53}$$

Substitution of Eq. (3.53) back into Eq. (3.52) yields the separated equations

$$\frac{g''}{g} + C^2 = \frac{f''}{f} = \lambda^2 \tag{3.54}$$

For the solid rocket motor, the only physically feasible choice is $\lambda = 0$. For this case, the solution takes the form of

$$\psi_0 = (C_1 x + C_2) \left[C_3 \sin(Cy) + C_4 \cos(Cy) \right] \tag{3.55}$$

To facilitate the application of the boundary conditions, Eq. (3.55) is differentiated with respect to x to get

$$C_1 C_3 \sin(Cy) + C_1 C_4 \cos(Cy) \tag{3.56}$$

and with respect to y to find

$$(C_1 x + C_2)\left[CC_3 \cos(Cy) - CC_4 \sin(Cy)\right] \tag{3.57}$$

These allow direct application of the boundary conditions.

Equation (3.34) is first applied by evaluating Eq. (3.56) at $(x, 0)$:

$$C_1 C_4 = 0 \tag{3.58}$$

To determine which constant must vanish, Eq. (3.36) is invoked to find

$$C_1 C_3 \sin(C) = 1 \tag{3.59}$$

One deduces that C_1, C_3, and C cannot be equal to zero, as this would make satisfying the boundary condition impossible. This reduces Eq. (3.58) to $C_4 = 0$. C_2 is determined by administering Eq. (3.37) such that

$$CC_2 C_3 \cos(Cy) = 0 \tag{3.60}$$

Since it has already been determined that C_3 and C could not equal zero, the only solution that allows this boundary condition to be satisfied for all values of y is $C_2 = 0$. Equation (3.35) is used to determine the constant C. Hence,

$$CC_1 C_3 x \cos(C) = 0 \tag{3.61}$$

To satisfy both this boundary condition and the one specified in Eq. (3.59), one must set $\cos(C) = 0$. For the cosine term to vanish, it is necessary that $C = \frac{\pi}{2}$, leaving the constants C_1 and C_3 yet to be determined. However, C_1 and C_3 can now be lumped together into a single constant because they always appear multiplying each other in the solution. Using Eq. (3.59) yields that $C_1 C_3 = 1$, which fully determines Eq. (3.55) to be

$$\psi_0 = x \sin\left(\frac{\pi y}{2}\right) \tag{3.62}$$

This result is the two-dimensional analog to the axisymmetric result obtained by Culick.[4]

3.2.3 First Order Thermodynamic Variables

Determining the first order pressure is a straightforward process once the leading order stream function is known. The first step is to remove the vorticity term from the equation by substituting the relation from Eq. (3.51):

$$-\frac{\nabla p_1}{\gamma} = \nabla\left(\frac{\nabla\psi_0 \cdot \nabla\psi_0}{2}\right) + \frac{\pi^2}{4}\psi_0 \nabla\psi_0 \tag{3.63}$$

It is possible to further simplify Eq. (3.63) via the identity $\psi_0 \nabla\psi_0 = \frac{1}{2}\nabla\psi_0^2$, hence

$$-\frac{\nabla p_1}{\gamma} = \nabla\left(\frac{\nabla\psi_0 \cdot \nabla\psi_0}{2} + \frac{\pi^2}{8}\psi_0^2\right) \tag{3.64}$$

This equation may be directly integrated with ψ_0 from Eq. (3.62) substituted, to eliminate the ψ_0 terms, thus formulating the first order pressure purely in terms of the geometry of the solution domain.

$$-\frac{p_1}{\gamma} = \frac{1}{2}\left[\sin^2\left(\frac{\pi y}{2}\right) + \frac{\pi^2 x^2}{4}\cos^2\left(\frac{\pi y}{2}\right)\right] + \frac{\pi^2 x^2}{8}\sin^2\left(\frac{\pi y}{2}\right) \tag{3.65}$$

From Eq. (3.65), by rearranging the equation for p_1 and using trigonometry identities, the final answer for the first order pressure is found to be

$$p_1 = -\frac{\gamma}{2}\left[\sin^2\left(\frac{\pi y}{2}\right) + \frac{\pi^2 x^2}{4}\right] \tag{3.66}$$

Determining the first order density and temperature is also straightforward, requiring only the substitution of Eq. (3.66) into Eqs. (3.24) and (3.28) respectively. One obtains

$$\rho_1 = -\frac{1}{2}\left[\sin^2\left(\frac{\pi y}{2}\right) + \frac{\pi^2 x^2}{4}\right] \tag{3.67}$$

and

$$T_1 = \frac{1-\gamma}{2}\left[\sin^2\left(\frac{\pi y}{2}\right) + \frac{\pi^2 x^2}{4}\right] \tag{3.68}$$

This result follows from the isentropic path functions that relate the thermodynamic variables. Polytropic equation of state models may improve the accuracy of the overall flow model but for the first attempt at a compressible solution, the isentropic relations are deemed satisfactory to bring closure to the solution.

3.3 First Order Solution

The first order solution procedure follows the same general outline as the leading order's. It requires that the vorticity transport equation be first solved, followed by solution of the vorticity stream function equation, and then the isentropic equations are introduced to bring closure to the thermodynamic variables. While this sounds easily extensible, the first order equations will be seen to present greater challenges than the leading order equations: the latter are simply the incompressible equations for the slab rocket flow. It is not until the first order corrections are found, that the effects of compressibility on the flow field can be determined.

3.3.1 First Order Vorticity Transport Solution

As in the case for the leading order solution, the vorticity transport equation is first used to determine the relationship between vorticity and stream function. To that end, Eq. (3.17) is examined to derive this relationship. The first simplification is that p_1 and ρ_1 differ only by a constant, γ. The result of this is that the right hand side of Eq. (3.17) vanishes since the evaluation of the cross product between two colinear vectors is zero. This simplifies the equation to

$$\nabla \times (\mathbf{U}_0 \times \mathbf{\Omega}_1) + \nabla \times (\mathbf{U}_1 \times \mathbf{\Omega}_0) = 0 \tag{3.69}$$

The vector operations are then expanded to find

$$\frac{\partial}{\partial x}(u_0\Omega_1 + u_1\Omega_0) + \frac{\partial}{\partial y}(v_0\Omega_1 + v_1\Omega_0) = 0 \tag{3.70}$$

To get the desired relationship between the first order vorticity and the stream function, Eqs. (3.6)−(3.9) and Eq. (3.51) may be substituted; one gets

$$\begin{aligned}\frac{\partial}{\partial x}&\left[\frac{\partial\psi_0}{\partial y}\Omega_1 + \left(\frac{\partial\psi_1}{\partial y} - \rho_1\frac{\partial\psi_0}{\partial y}\right)\frac{\pi^2}{4}\psi_0\right] \\ &+\frac{\partial}{\partial y}\left[-\frac{\partial\psi_0}{\partial x}\Omega_1 + \left(\rho_1\frac{\partial\psi_0}{\partial x} - \frac{\partial\psi_1}{\partial x}\right)\frac{\pi^2}{4}\psi_0\right] = 0\end{aligned} \tag{3.71}$$

The derivatives may be evaluated and the expanded equation simplified after cancellation of some of the terms to give

$$\frac{\partial\Omega_1}{\partial x}\frac{\partial\psi_0}{\partial y} - \frac{\partial\Omega_1}{\partial y}\frac{\partial\psi_0}{\partial x} = \frac{\pi^2}{4}\left[\psi_0\left(\frac{\partial\rho_1}{\partial x}\frac{\partial\psi_0}{\partial y} - \frac{\partial\rho_1}{\partial y}\frac{\partial\psi_0}{\partial x}\right) + \frac{\partial\psi_1}{\partial x}\frac{\partial\psi_0}{\partial y} - \frac{\partial\psi_1}{\partial y}\frac{\partial\psi_0}{\partial x}\right] \tag{3.72}$$

At first glance this equation appears intractable. The method of determining a relation without fully solving the equation is not practical. However, further simplification is possible if one realizes that the first order vorticity is an extension of the leading order term. It is not enough to let $\Omega_1 = \frac{\pi^2}{4}\psi_1$ as this expression does not satisfy Eq. (3.69). To make the

proper simplification one lets

$$\Omega_1 = \frac{\pi^2}{4}\psi_1 + \Omega_c \tag{3.73}$$

where Ω_c is an additional correction function required to satisfy the governing equation. When Eq. (3.73) is substituted back into Eq. (3.72) the following simplified equation results

$$\frac{\partial \Omega_c}{\partial x}\frac{\partial \psi_0}{\partial y} - \frac{\partial \Omega_c}{\partial y}\frac{\partial \psi_0}{\partial x} = \frac{\pi^2}{4}\psi_0\left(\frac{\partial \rho_1}{\partial x}\frac{\partial \psi_0}{\partial y} - \frac{\partial \rho_1}{\partial y}\frac{\partial \psi_0}{\partial x}\right) \tag{3.74}$$

Since ρ_1 has been previously determined, and ψ_0 is known, this equation can be solved by integration to yield:

$$\Omega_c = \pm\frac{\pi^2 x}{32}\left[\pi^2 x^2 \sin\left(\frac{\pi y}{2}\right) + 4\sin^2\left(\frac{\pi y}{2}\right)\right] + f(\psi_0) \tag{3.75}$$

where f is an as-yet specified function of the stream function. This function will be used later to ensure that the first order equation is able to satisfy all of the requisite boundary conditions.

3.3.2 First Order Vorticity Solution

With the addition of Eq. (3.75), it is possible to then examine Eq. (3.13). Substitution of Eqs. (3.51), (3.62), (3.67), and (3.75) into Eq. (3.13) gives

$$\begin{aligned}\frac{\partial^2 \psi_1}{\partial y^2} + \frac{\partial^2 \psi_1}{\partial x^2} + \frac{\pi^2}{4}\psi_1 = \\ \nabla\left\{-\frac{1}{2}\left[\sin^2\left(\frac{\pi y}{2}\right) + \frac{\pi^2 x^2}{4}\right]\right\}\cdot\nabla\left[x\sin\left(\frac{\pi y}{2}\right)\right] \\ +\frac{\pi^2}{8}\left[\sin^2\left(\frac{\pi y}{2}\right) + \frac{\pi^2 x^2}{4}\right] - \frac{\pi^2 x}{32}\left[\pi^2 x^2\sin\left(\frac{\pi y}{2}\right) + 4\sin^2\left(\frac{\pi y}{2}\right)\right] + f(\psi_0)\end{aligned} \tag{3.76}$$

After expansion of the vector operator and taking the dot-products, and with the trigonometric simplification, the single scalar equation results

$$\frac{\partial^2 \psi_1}{\partial y^2} + \frac{\partial^2 \psi_1}{\partial x^2} + \frac{\pi^2}{4}\psi_1 = -\frac{\pi^2 x}{4}\sin\left(\frac{\pi y}{2}\right)\left[\cos(\pi y) + 1 - \frac{\pi^2 x^2}{4}\right] - f(\psi_0) \tag{3.77}$$

Equation (3.77) uses the negative root of the vorticity correction function. The negative root is selected because it is the only root that will satisfy the boundary conditions, as will be shown later. Since $f(\psi_0)$ is used to satisfy the boundary conditions, it is required that the $f(\psi_0)$ term obeys a mathematical form consistent with the other term of the right hand side. To this end, $f(\psi_0)$ is defined as

$$f(\psi_0) = A_1 x \sin\left(\frac{\pi y}{2}\right) + A_2 x^3 \sin^3\left(\frac{\pi y}{2}\right) \tag{3.78}$$

where A_1 and A_2 are constants to be determined. To simplify bookkeeping in the remainder of the text, we let $\eta \equiv \frac{1}{2}\pi y$. Next, a general solution is assumed,

$$\psi_1(x,\eta) = xG(\eta) + x^3 H(\eta) \tag{3.79}$$

This general solution is the result of substituting multiple trial functions into the governing equations and testing to see if the function could provide a valid solution that satisfies the governing equations. In retrospect, this particular choice makes sense as it mirrors the extension of the leading order solution. Substitution of this form for ψ_1 back into Eq. (3.77) gives

$$\begin{aligned}\frac{\pi^2}{4}\left[x\left(G'' + G\right) + x^3\left(H'' + H\right)\right] + 6xH = \\ -\frac{\pi^2 x}{4}\sin\left(\frac{\pi y}{2}\right)\left[\cos(\pi y) + 1 - \frac{\pi^2 x^2}{4}\right] + A_1 x \sin\eta + A_2 x^3 \sin^3\eta\end{aligned} \tag{3.80}$$

where the primed quantities represent derivatives with respect to η. Equation (3.80) is further simplified by grouping all terms in powers of x. One gets

$$\begin{aligned}x^3\left[\frac{\pi^2}{4}\left(H'' + H - \frac{\pi^2}{4}\sin\eta\right) - A_1\sin^3\eta\right] \\ +x\left[\frac{\pi^2}{4}\left(G'' + G + \sin\eta + \cos 2\eta \sin\eta\right) + 6h - A_2\sin\eta\right] = 0\end{aligned} \tag{3.81}$$

In order for Eq. (3.81) to be true for all values of x, the bracketed quantites multiplying both the x^3 and x terms must vanish. The partial differential equation can now be written as two ordinary differential equations:

$$H'' + H = \frac{\pi^2}{4}\sin\eta + A_1 \sin^3\eta \tag{3.82}$$

and

$$G'' + G = \frac{4}{\pi^2}\left(A_2 \sin\eta - 6h\right) - \sin\eta - \cos 2\eta \sin\eta \tag{3.83}$$

Note that Eq. (3.82) is written only in terms of H, so it can be solved first to determine h and subsequent substitution into Eq. (3.83) brings closure to that equation.

The solution for Eq. (3.82) follows a similar procedure to that of the separated variable equation, Eq. (3.54). The only complication is that the equation is nonhomogeneous, so a particular solution must be obtained in addition to a general solution. The solution for Eq. (3.82) is found to be

$$\begin{aligned} H = {} & C_1 \cos\eta + C_2 \sin\eta \\ & + \frac{\pi^2}{16}\left(\cos\eta \sin 2\eta - 2\eta\cos\eta - \sin\eta - \cos 2\eta \sin\eta\right) \\ & + \frac{A_1}{8\pi^2}\left(\cos 4\eta \sin\eta + 8\cos\eta\sin 2\eta - 12\eta\cos\eta - 4\cos 2\eta\sin\eta - \cos\eta\sin 4\eta\right) \end{aligned} \tag{3.84}$$

where C_1 and C_2 are two more constants that must be determined. This solution is then substituted to the right hand side of Eq. (3.83) so that all of the nonhomogeneous terms are determined. The solution to Eq. (3.82) is determined identically to Eq. (3.83) with the

differences due to the additional nonhomogeneous terms. One finds

$$\begin{aligned}
G = & C_3 \cos\eta + C_4 \sin\eta \\
& + \frac{A_1}{16\pi^4}[144\left(\eta\cos\eta + \eta\cos\eta\cos 2\eta + \eta^2\sin\eta + \eta\sin\eta\sin 2\eta\right) \\
& + 156\cos 2\eta\sin\eta - 132\cos\eta\sin 2\eta + 6\left(\cos 4\eta\sin\eta - \cos\eta\sin 4\eta\right)] \\
& + \frac{A_2}{\pi^2}[\cos\eta\sin 2\eta - 2\eta\cos\eta - \cos 2\eta\sin\eta] \\
& - \frac{6C_1}{\pi^2}[\cos\eta\cos 2\eta + 2\eta\sin\eta + \sin\eta\sin 2\eta] \\
& + \frac{6C_2}{\pi^2}[\cos 2\eta\sin\eta + 2\eta\cos\eta - \cos\eta\sin 2\eta] \\
& + \frac{1}{16}[12\left(\eta\cos\eta\cos 2\eta + \eta^2\sin\eta + \eta\sin\eta\sin 2\eta\right) + 10\cos 2\eta\sin\eta \\
& - 6\cos\eta\sin 2\eta + 4\eta\cos\eta + \cos 4\eta\sin\eta - \cos\eta\sin 4\eta]
\end{aligned} \tag{3.85}$$

Thus, two arbitrary constants of integration, C_3 and C_4 are added to the solution, giving a total of six arbitrary constants that need to be determined. The relationships for h and g can be substituted back into (3.79) to yield

$$\begin{aligned}
\psi_1 = & \frac{x}{16\pi^4}(-2\cos\eta\{12A_1\eta(\pi^2x^2 - 12) \\
& + \pi^2[16A_2\eta + \pi^4x^2\eta + 48(C_1 - 2\eta C_2) - 8\pi^2(\eta + x^2C_1 + C_3)]\} \\
& + 4\sin\eta\{3A_1[\pi^2x^2 + 12(\eta^2 - 1)] + \pi^2[4A_2 - 24(2\eta C_1 + C_2) \\
& + \pi^2(-2 + 3\eta^2 + 4x^2C_2 + 4C_4)]\} + \sin 3\eta[\pi^4 + 2A_1(\pi^2x^2 + 3)])
\end{aligned} \tag{3.86}$$

While Eq. (3.86) does not appear to be the elegant solution one hopes for, there is potential for simplification from administering the boundary conditions. Despite the presence of additional unknowns, these follow the same agendum as the leading order coefficients. One first examines the no flow across the symmetry plane from Eq. (3.42), recalling that it is evaluated at $(x, 0)$,

$$-\frac{6C_1}{\pi^2} + C_3 + 3x^2C_1 = 0 \tag{3.87}$$

In order for this equation to be true for all values of x the coefficient multiplying the x^2 term must vanish. Thus,

$$C_1 = 0 \tag{3.88}$$

One may also set $\psi = 0$ along the symmetry plane, and also across the headwall. At the onset, both ψ_0 and ψ_1 must vanish at the origin. Hence,

$$C_3 = 0 \tag{3.89}$$

Revisiting Eq. (3.43) with the reduced number of terms, we have

$$\begin{aligned} &\frac{x^3}{16\pi^4}\left(6A_1\pi^4 + \frac{\pi^8}{2}\right) \\ &\quad + \frac{x}{16\pi^4}\left[-72A_1\pi^2 + 8A_2\pi^4 - 4\pi^6 + 4\left(18A_1\pi^2 + \frac{3\pi^6}{2}\right) - 48\pi^4 C_2\right] = 0 \end{aligned} \tag{3.90}$$

This equation in turn may be separated into two equations, such that Eq. (3.90) holds for all values of x, for which

$$A_1 = -\frac{\pi^4}{12} \tag{3.91}$$

and

$$8A_2\pi^4 + 2\pi^6 - 48\pi^4 C_2 = 0 \tag{3.92}$$

Leaving Eq. (3.92) momentarily, it is advantageous to apply the boundary condition from Eq. (3.44),

$$x^2\left(3C_2 - \frac{\pi^2}{32}\right) + C_4 + \frac{23}{32} + \frac{A_2}{\pi^2} - \frac{6C_2}{\pi^2} = 0 \tag{3.93}$$

This equation can then be segregated into a requirement consisting of

$$C_2 = \frac{\pi^2}{96} \tag{3.94}$$

and

$$C_4 + \frac{21}{32} + \frac{A_2}{\pi^2} = 0 \tag{3.95}$$

Solving Eqs. (3.92) and (3.95) simultaneously determines the final two constants

$$A_2 = -\frac{3\pi^2}{16} \tag{3.96}$$

$$C_4 = -\frac{15}{32} \tag{3.97}$$

Substitution of the constants back into Eq. (3.86) and reverting back to the natural coordinate y gives the simplified result that

$$\psi_1 = -\frac{x}{48}\sin\left(\frac{\pi y}{2}\right)\left\{\pi^2 x^2\left[3+\cos\left(\pi y\right)\right]+3\left[7-\cos\left(\pi y\right)\right]\right\} \tag{3.98}$$

3.3.3 Second Order Thermodynamic Variables

In order to determine the second order pressure term, one may expand the vector equation presented in Eq. (3.21) into two scalar equations:

$$\begin{aligned}\frac{\partial p_2}{\partial x} = &-\gamma\frac{\partial}{\partial x}\left\{\frac{\partial\psi_0}{\partial x}\frac{\partial\psi_1}{\partial x}+\frac{\partial\psi_0}{\partial y}\frac{\partial\psi_1}{\partial y}-\rho_1\left[\left(\frac{\partial\psi_0}{\partial x}\right)^2+\left(\frac{\partial\psi_0}{\partial y}\right)^2\right]\right\}\\ &+\gamma\left\{\frac{1}{2}\rho_1\frac{\partial}{\partial x}\left[\left(\frac{\partial\psi_0}{\partial x}\right)^2+\left(\frac{\partial\psi_0}{\partial y}\right)^2\right]+\Omega_0\frac{\partial\psi_1}{\partial x}+\Omega_1\frac{\partial\psi_0}{\partial x}\right\}\end{aligned} \tag{3.99}$$

and

$$\begin{aligned}\frac{\partial p_2}{\partial x} = &-\gamma\frac{\partial}{\partial y}\left\{\frac{\partial\psi_0}{\partial x}\frac{\partial\psi_1}{\partial x}+\frac{\partial\psi_0}{\partial y}\frac{\partial\psi_1}{\partial y}-\rho_1\left[\left(\frac{\partial\psi_0}{\partial x}\right)^2+\left(\frac{\partial\psi_0}{\partial y}\right)^2\right]\right\}\\ &+\gamma\left\{\frac{1}{2}\rho_1\frac{\partial}{\partial y}\left[\left(\frac{\partial\psi_0}{\partial x}\right)^2+\left(\frac{\partial\psi_0}{\partial y}\right)^2\right]+\Omega_0\frac{\partial\psi_1}{\partial y}+\Omega_1\frac{\partial\psi_0}{\partial y}\right\}\end{aligned} \tag{3.100}$$

Equations (3.99) and (3.100) may be integrated, yielding

$$p_2 = \frac{\gamma\pi^2x^2}{128}(13-\cos 2\pi y)-\frac{\gamma\pi^4x^4}{384}+f_1(y) \tag{3.101}$$

and

$$p_2 = -\frac{\gamma}{16}\left(\cos\pi y + \cos^2\pi y\right) - \frac{\gamma\pi^2 x^2}{64}\cos^2\pi y + f_2(x) \tag{3.102}$$

in x and y respectively. After examining the two solutions and applying the trigonometric identity, $\cos 2a = 2\cos^2 a - 1$, it is possible to combine Eqs. (3.101) and (3.102) to determine the solution to the second order. One gets

$$p_2 = -\frac{\gamma}{16}\left(\cos\pi y + \cos^2\pi y\right) + \frac{\gamma\pi^2 x^2}{64}(7 - \cos^2\pi y) - \frac{\gamma\pi^4 x^4}{384} \tag{3.103}$$

Determining the second order density term is simply a matter of substituting the pressure terms from Eqs. (3.66) and (3.103) back into Eq. (3.25). One extracts

$$\begin{aligned}\rho_2 = {} & \frac{1}{32}\left[1 - \gamma + 2(\gamma - 2)\cos\pi y - (\gamma + 1)\cos^2\pi y\right] \\ & + \frac{\pi^2 x^2}{64}\left[9 - 2\gamma + 2(\gamma - 1)\cos\pi y - \cos^2\pi y\right] + \frac{\pi^4 x^4}{384}(2 - 3\gamma)\end{aligned} \tag{3.104}$$

Similarly the second order temperature becomes

$$T_2 = \frac{1 - \gamma}{192}\left[6(1 + 3\cos^2\pi y) + 3\pi^2 x^2(-5 - 2\cos\pi y + \cos^2\pi y) + 2\pi^4 x^4\right] \tag{3.105}$$

after similar substitutions.

Chapter 4

Results and Discussion

Having obtained the closed form relations for the compressible slab motor it is necessary that these expressions be used to clearly illustrate the effects of compressibility on the motor flow field, performance, and design criteria. In order to fully appreciate the physics of the flow that the mathematical treatment captures, one must first verify and validate the relationships presented here to ensure that they make physical sense. In this spirit, both a numerical and an experimental verification program are applied to the present study to verify the relationships uncovered in the previous sections.

4.1 Critical Length Calculation

To facilitate comparisons to past results both analytical and experimental, it is convenient to normalize the axial distance by the critical length of the motor. The critical length of a motor is defined as the distance, measured from the head end to where the flow reaches a sonic condition. For ease of calculation, the maximum axial velocity will be used to calculate the critical length, because this will be the first point in the flow that reaches a sonic condition along the center-axis. Obtaining the axial velocity and temperature at the

center-axis from the stream function yields:

$$u_c = u(x,0) = M_w\left(\frac{\pi x}{2}\right) - M_w^3\frac{\pi x}{48}\left(9-\pi^2x^2\right) \tag{4.1}$$

and

$$T_c = T(x,0) = 1 + M_w^2\frac{\gamma-1}{8}\left(\pi^2x^2\right) - M_w^4\frac{\gamma-1}{96}\left(12-9\pi^2x^2+\pi^4x^4\right) \tag{4.2}$$

One can retain all terms in the expanded velocities and temperatures to recover an accurate expression of the choke length:

$$M_w\frac{\pi x}{2} - M_w^3\frac{\pi x M_w^3}{96}\left(18-2\pi x^2\right) = \sqrt{1 - M_w^2\frac{(\gamma-1)}{8}\pi^2x^2 - M_w^4\frac{(\gamma-1)}{96}\left(12-9\pi^2x^2+\pi^4x^4\right)} \tag{4.3}$$

The equation of interest is a cubic equation with large coefficients,

$$\frac{M_w^6\pi^6}{2304}x^6 + \frac{M_w^4\pi^4}{384}\left[4(\gamma+1)-3M_w^2\right]x^4 + \frac{M_w^2\pi^2}{256}\left[32(\gamma+1)-24(\gamma+1)M_w^2+9M_w^4\right]x^2 + \frac{M_w^4(\gamma-1)}{8} - 1 = 0 \tag{4.4}$$

which has the real, positive root

$$x_s^{(2)} = \frac{1}{\pi M_w}\sqrt{\frac{9M_w^4+6M_w^2\left[\phi^{\frac{1}{3}}-4(\gamma+1)\right]+\phi^{\frac{2}{3}}-8\phi^{\frac{1}{3}}(\gamma+1)+32(2\gamma^2+\gamma-1)}{\phi^{\frac{1}{3}}}} \tag{4.5}$$

where ϕ is

$$\begin{aligned}\phi = & \\ & -[36M_w^4(\gamma-7) - 288M_w^2(\gamma^2-\gamma-2) + 128(4\gamma^3+3\gamma^2-6\gamma-14)] \\ & +12[-64M_w^4(11\gamma^4+85\gamma^3+63\gamma^2-76\gamma-137) \\ & +4608M_w^2(\gamma^4+2\gamma^3+\gamma^2-3\gamma-3) \\ & -1024(3\gamma^4+14\gamma^3+6\gamma^2-18\gamma-22)]^{\frac{1}{2}}\end{aligned} \tag{4.6}$$

Equation (4.5) is only weakly dependent on the Mach number under the radical, so to that end one can find a more manageable approximate expression for the sonic length. Namely,

$$x_{sa}^{(2)} = \frac{1}{\pi M_w}\sqrt{\frac{\phi_a^{\frac{2}{3}} - 8\phi_a^{\frac{1}{3}}(\gamma+1) + 32(2\gamma^2+\gamma-1)}{\phi_a^{\frac{1}{3}}}} \tag{4.7}$$

where

$$\phi_a = -[128(4\gamma^3+3\gamma^2-6\gamma-14)] + 12\sqrt{-1024(3\gamma^4+14\gamma^3+6\gamma^2-18\gamma-22)} \tag{4.8}$$

Equation (4.7) is accurate to the third decimal place when compared to the similar full expression of the sonic length for most injection Mach numbers for rocket applications. For a comparison of the various orders of accuracy of the critical length, the reader is referred to the Appendix.

4.2 Computational Verification of the Analytical Solution

In order to ensure that the perturbation expansion is valid, a numerical verification is performed. Version 6.1 of the Fluent® computational fluid dynamics (CFD) solver provides a segregated, two-dimensional, double precision, compressible solver that is used to provide the numerical comparisons. Laminar flow and Spalart-Allmaras models are used to account for viscosity effects in the CFD calculations. A rectangular geometry with a half height of 1 cm and a length of 45 cm is chosen to model the slab geometry since this matches the conditions of Traineau.[5] The solver provides data for the same top half of the slab motor as the analytical solution, which can be mirrored across the center-axis. A uniform mass injection is imposed on the sidewalls of 13 kg m^{-2} s^{-1}, providing a close approximation of the constant velocity injection used in the perturbation analysis. The injection gas is assumed to be air with an injection temperature of 260 K, molecular weight of 29 kg $kmol^{-1}$, dynamic viscosity of 1.66×10^{-5} kg m^{-1} s^{-1}, and a ratio of specific heats of 1.4.

4.2.1 Thermodynamic Properties

The first verification provides the thermodynamic properties along the symmetry plane of the chamber, namely, the pressure and temperature. These parameters are chosen for their ease of calculation both numerically and analytically, as well as for their ability to provide comparisons along the entire length of the simulated motor.

Figure 4.1(a) compares the center-plane pressure profiles obtained using $\gamma = 1.4$. All of the analytical and computational models agree near the headwall of the chamber. Examining the solution presented here, good agreement is observed near the headwall, with deviations from the numerical simulation appearing as the flow progresses to the aft end. It is interesting to note that the present solution more closely matches the Spalart-Allmaras model than the laminar flow model. This can be attributed to the quasi-viscous nature of the flow, driven by the normal injection condition at the walls. Even though the present solution is inviscid, it can approximate some features of weakly sheared viscous flow. Had a viscous model been used, one would have expected the deviation of pressures at the aft end to be further reduced.

The temperature comparison in Figure 4.1(b) presents a slightly different contrast. As in the pressure comparison, the agreement at the headwall of the chamber is excellent since the head end Mach number is very small, but the compressibility effects on temperature become more visible as the flow progresses past the halfway point in the motor. The solution obtained in the present study approaches the numerical solutions as the flow nears the exit of the motor. The present analysis more closely follows the laminar numerical model, than the more elaborate turbulent model. This is not unexpected and can be accounted for by two causes. The first is that while the normal injection condition at the walls provides a quasi-viscous behavior, it does not account for any thermal effects that a viscous flow may introduce. Thus, the present analytical model would be expected to under-predict the center-axis temperature. The second cause is that the energy model used to determine the temperature, namely isentropic flow, is restrictive. Relaxing the isentropic condition would no doubt lead to a more accurate prediction of the center-axis temperature.

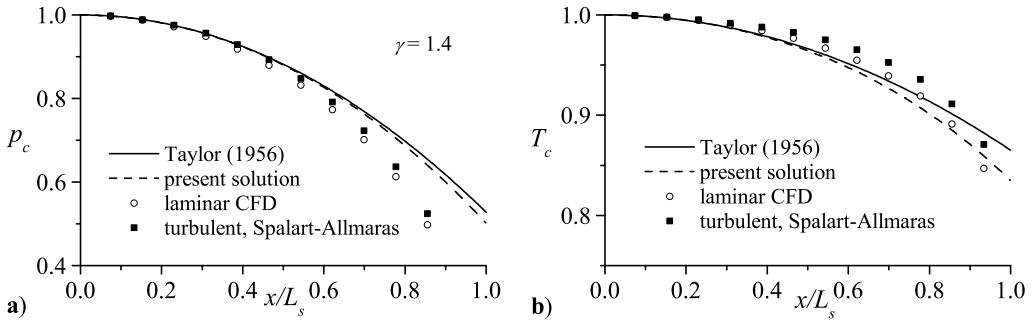


Figure 4.1: Computational verification of the center-axis pressures and temperatures.

4.2.2 Velocity Verification

It is also of interest to compare the predicted velocity profiles at various points in the motor chamber. Since high velocities can lead to changes in motor performance, it is important that these variations are correctly accounted for. In order to get good comparisons throughout the motor, comparisons are made for the center-axis velocities.

The center-axis comparison in Figure 4.2 shows some interesting features and generally good agreement with the numerical results. The present work matches well early in the chamber, but falls below the numerical predictions near the end of the chamber. This difference can be accounted for by the lack of viscous effects in our formulation. While it is true with the normal injection condition that some aspects of the solution may approximate a viscous model, the effect of the normal injection is decreasing as the flow moves downstream and toward the center-axis. The result is an inviscid centerline flow with a slightly different shape than one accounting for viscosity. If the viscous losses were accounted for, the center-axis velocity would trend toward closer agreement with the numerical results.

4.3 Theoretical and Experimental Comparisons

Flow in a rectangular channel has been a topic studied in a number of different applications and as a result there is a wealth of theoretical and experimental data available to make comparisons against. Even in the relatively narrow application of the slab rocket motor,

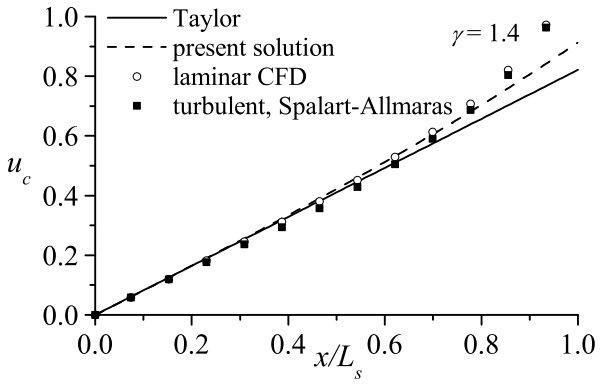


Figure 4.2: Comparison of predicted center-axis velocity with numerical results.

studies by Traineau *et. al.*[5] and Gany and Aharon[15] provide both theoretical and experimental results. In the interest of clarity, Taylor's incompressible solution for the slab may also be used as a benchmark.

4.3.1 Pressure Comparison

A baseline for comparison is the pressure distribution along the center-axis of the motor, shown in Figure 4.3. Traineau presents both a one-dimensional, and a pseudo-two-dimensional analysis using a stream tube analysis, and also a set of experimental data to compare to the theory. The results here are somewhat surprising. The one-dimensional model appears to closely match the experimental data for the center-axis pressure. Traineau notes the same, along with reasons why the two-dimensional numerical simulation under-predicts the experimental data. It is possible that the introduction of viscous effects would lower the axial gradient, thus explaining the two-dimensional results from Traineau being lower than the observed experimental data. However, it does not completely explain why the one-dimensional model matches the center-axis pressure prediction so well, while being less accurate for other variables of interest. It is speculated that the effects of viscosity cancel in the one-dimensional model since the flow is injected along the center-axis. If this is the case, one would expect the relaxing of the inviscid condition to produce a shift down

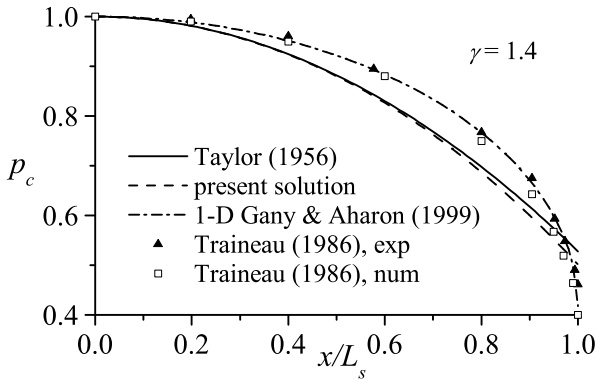


Figure 4.3: Comparison of center-axis pressures to former studies.

in the center-axis pressure, bringing the predicted pressure in line with experimental results.

4.3.2 Velocity Comparison

To assess compressibility effects on velocity profiles at varying locations in the motor, our solution will be compared to data from Traineau's experimental and computational study. This enables us to not only track the evolution predicted by the present model, but also to establish a comparison grounded in reality with the experimental results. Traineau's measurements are taken at various locations which, when normalized by the length of the motor, occur at approximately twenty percent increments of the total length beginning with forty percent.

The agreement of the asymptotic formulation with the experimental data, now shown in Figure 4.4, is encouraging. In all locations, the compressible model presented here more closely agrees with the experimental data than the incompressible model. Near the headwall of the motor both the incompressible and compressible models bear close resemblance to the experimental data, confirming that some length is required for the flow to develop to the point where compressibility effects become non-negligible.

The axial velocity profiles evolve as the flow progresses through the motor. Near the headwall, the flow is nearly incompressible, following the sinusoidal profile predicted by

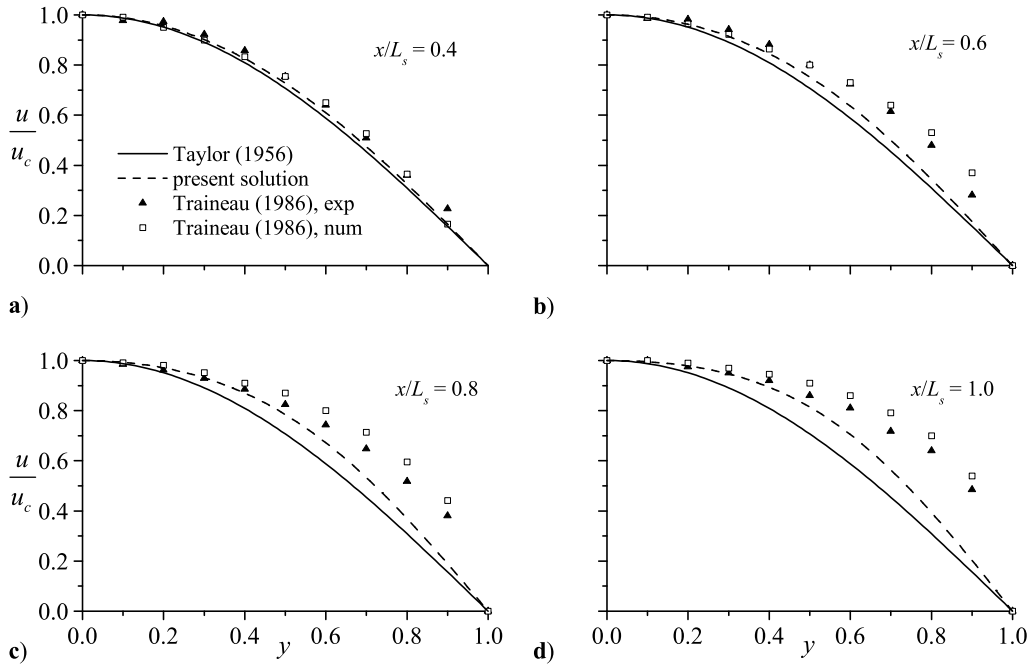


Figure 4.4: Comparison of axial velocities at various motor locations.

Taylor. The incompressible Taylor velocity is invariant in Figure 4.4 because of the normalization used. However, as the flow travels further downstream, the velocity profile steepens, thus indicating that greater shearing action is being experienced in the viscous solutions, in addition to the displacement effect which characterizes the inviscid flow. This steepening is found in both the experimental data and the computational verification of Traineau. It has been posited previously by Balakrishnan *et al.*[14] that the steepening effects could be attributed to compressibility or turbulent viscous effects. Using the present model as a guide, one may see that at least a portion of the steepening effect can be attributed to the correct accounting for compressibility. While the agreement between the present model and the experimental data is not perfect, one would expect that properly accounting for viscosity and possible turbulent effects would further steepen the axial velocity profile, thus bringing it closer to agreement with the experimental measurements.

Since the work of Balakrishnan *et al.*[8] is still the most widely cited compressible study of rocket motors, a comparison to the present inquiry is made in Figure 4.5. Figure 4.5(a)

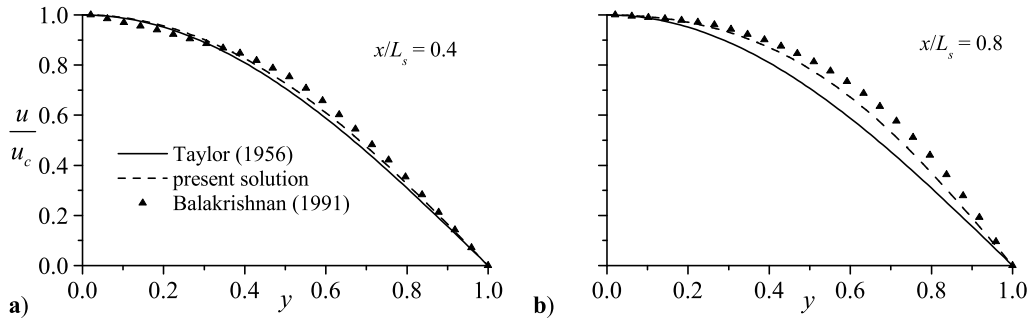


Figure 4.5: Axial velocity comparison with Balakrishnan *et al.*.

depicts the velocity profile at $x/L_s = 0.4$, before the effects of compressibility become dominant. Here, the velocity profiles of the incompressible baseline, the present work, and the Balakrishnan numerical study are all in close agreement. In Figure 4.5(b), the flow nears the sonic length at $x/L_s = 0.8$ and compressibility effects become more pronounced. The present analysis shows good agreement with the results of Balakrishnan's study. While the present thesis slightly underpredicts the Balakrishnan work, it has the benefit of being a closed form, analytical solution, whereas Balakrishnan must integrate numerically to produce similar results.

4.4 Streamlines

The behavior of the streamlines is illustrated in Figure 4.6. The solid lines depict the incompressible streamlines and the dotted lines show the effects of compressibility. When compressibility effects are accounted for, the streamlines turn more rapidly, providing a steeper profile. As the injection velocity is increased, the behavior becomes more pronounced, and deviations from the incompressible condition are observed earlier in the flow. As the injection Mach number is increased, the motor length required for the flow to reach sonic conditions is decreased. This behavior is reflective of a strong correlation between the critical motor length and the injection Mach number as alluded to in Sec. 4.1.

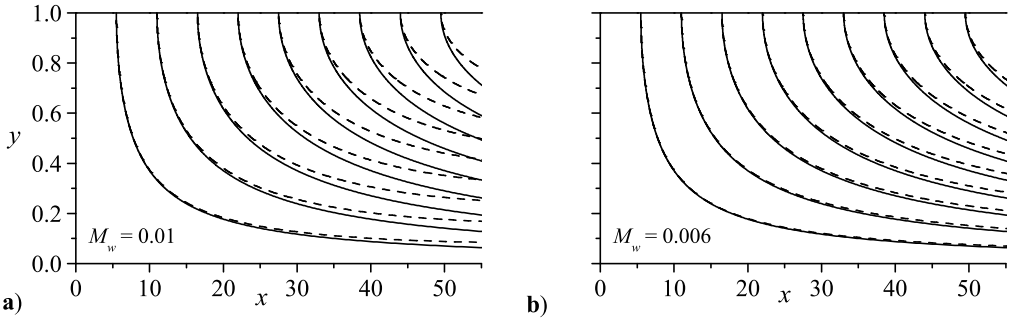


Figure 4.6: The effects of compressibility on the streamlines of a slab rocket motor.

The streamline plots also show the effects of compressibility as the flow progresses through the motor. Near the headwall, the effects of compressibility are relatively negligible, a behavior that has been previously observed in the numerical simulation. As the fluid travels toward the aft end and increases in speed, compressibility effects become more pronounced. Using the streamline plot as a guide, it is possible to calculate the axial location where the magnification of the velocity by compressibility becomes so large that it must be taken into account.

4.5 Compressible Design Criterion

This leads to an important question that every motor designer must ask: Do I need to worry about compressibility effects in my design or can I safely work with an incompressible model? In an attempt to answer this question, one may look at a set of criteria for measuring the effects of compressibility. The first criterion is the compressibility ratio,

$$\chi_c = \frac{u(0,z)}{u_0(0,z)} \tag{4.9}$$

This is simply the ratio between the compressible and incompressible velocities. It represents the amplification of the center-axis velocity at a given location in the motor.

It is possible to obtain an analytical expression for the compressible amplification via substitution of Eqs. (3.1), (3.6), and (3.7) back into Eq. (4.9). These yield

$$\chi_c = 1 + \frac{1}{24} M_w^2 \left(\pi^2 x^2 - 9\right) \tag{4.10}$$

One way for a motor designer to effectively make use of the formulation in Eq. (4.10) is to introduce an acceptable difference, here labeled ϵ. If a designer knows that a compressible-incompressible velocity difference of up to 5% is acceptable, he may let $\chi_c = 1 + \epsilon$. With this substitution and subsequent simplifcation, Eq. (4.10) becomes

$$x_\epsilon = \sqrt{\frac{24\epsilon}{M_w^2 \pi^2} + \frac{9}{\pi^2}} \tag{4.11}$$

This gives an expression for the location in the motor where this level of difference of ϵ first occurs. However, for a designer looking to get a reasonable approximation, the $9/\pi^2$ may be ignored because the first term in the equation dominates for typical values expected in rocket design; one is left with

$$x_\epsilon = \frac{2\sqrt{6\epsilon}}{M_w \pi} \tag{4.12}$$

Conversely, if the geometry of the motor is fixed, the designer can get a rough approximation of the maximum injection Mach number by rearranging the equation to yield $2\sqrt{6\epsilon}/(\pi x)$. Since calculations of this type often degrade in the vicinity of the nozzle, it is common practice for a designer to specify that an error can be acceptable if it is limited to a small fraction of the motor length near the nozzle. To adjust for this, one may introduce $x = (1 - z)L$ where z is the fraction of the motor length where the error is acceptable (the last $\frac{1}{8}$ for example), and $L = L_0/a$ is the aspect ratio of the motor. This substitution yields the critical value

$$M_w^* = \frac{2\sqrt{6\epsilon}}{\pi(1 - z)L} \tag{4.13}$$

For example, if a designer decides that for a motor with a 0.1 m radius and 4 m length, a velocity difference of 10% is allowable in the last 1/8 of the motor, he can directly apply

Eq. (4.13) as follows:

$$M_w^* = \frac{2\sqrt{6(0.10)}}{\pi(1-0.125)40} = 0.0141 \tag{4.14}$$

So for this hypothetical motor, an injection Mach number of 0.0141 constitutes the maximum injection condition that the motor can have and still be modeled effectively with an incompressible model. Since this value is on the high side for most motors, an incompressible model will, for all intents and purposes, be acceptable for this motor.

The validity of these criteria are easily verifiable. The compressibility criteria set forth in Eqs. (4.12) and (4.13) are used to select the stream function plots shown in Figure 4.6. This is accomplished by allowing a five percent deviation in the last eighth of the motor. In Figure 4.6(a), a designer is well advised to absorb the extra complexity of the compressible model in favor of the more accurate flow field prediction. Just from a cursory examination of the streamlines, one may see significant deviations from the incompressible flow model almost immediately. In the second, less extreme case shown in Figure 4.6(b) the effects of compressibility are seen to be relatively negligible. Steepening of the streamlines is observed, but not in any degree that would alarm a potential designer.

4.6 Internal Ballistics

One of the advantages of the present approach is that because the primary variables are known at any position in the motor, it is possible to calculate secondary performance characteristics. More so than velocity profiles or streamline plots, these ballistics terms are at the heart of practical rocket analysis. To facilitate a practical use of this analysis, we determine some of the critical ballistics parameters with full analytical expressions.

4.6.1 Mass Flow Rate

First an expression for the total mass flowrate at any given cross-section is determined. For the steady case analyzed here, the general expression for the total mass flow rate in

non-dimensional terms is

$$\dot{m} = \int \rho u \, \mathrm{d}A = 2w \int_0^1 \rho u \, \mathrm{d}y \tag{4.15}$$

where $w = \bar{w}/a$. Substitution of the relations for ρ and u and completing the integration produces a lengthy equation, which however is easily programmable. A more compact approximate expression is presented here, after multiplying by the proper dimensional constants to ensure correct units. This equation is accurate to three decimal places for the range of operation for most motors.

$$\dot{m} = \frac{a_0 \rho_0 a^2}{2304} M_w w x (M_w^2 \pi^2 x^2 + 12) \left[M_w^4 \pi^4 x^4 (2 - 3\gamma) - 48 M_w^2 \pi^2 x^2 + 384 \right] + O(M_w^5) \tag{4.16}$$

4.6.2 Thrust Force

In order to continue with the ballistics study the thrust force generated by the rocket motor must be determined. The thrust force for a given motor length can be expressed as

$$F = \int \rho u^2 \, \mathrm{d}A = 2w \int_0^1 \rho u^2 \, \mathrm{d}y \tag{4.17}$$

which after substitution, integration, and dimensionalization becomes

$$\begin{aligned} F = {} & \frac{a_0^2 a^2 \rho_0}{1536} M_w^2 \pi^2 x^2 w \left(\frac{29}{4608} M_w^4 \pi^4 x^4 + \frac{7}{48} M_w^2 \pi^2 x^2 + 1 \right) \\ & \cdot \left[M_w^4 \pi^4 x^4 (2 - 3\gamma) - 48 M_w^2 \pi^2 x^2 + 384 \right] + O(M_w^5) \end{aligned} \tag{4.18}$$

Equation (4.18) is also an approximate expression for the thrust force, accurate to four significant digits.

4.6.3 Specific Impulse

Even as approximate expressions, Eqs. (4.16) and (4.18) are slightly cumbersome to handle. However, when the thrust force is divided by the mass flux and the standard acceleration

of gravity at sea level, one can determine the specific impulse in units of seconds.

$$I_s = \frac{F}{\dot{m} g_0} = \frac{a_0}{3072 g_0} M_w \pi^2 x (M_w^2 \pi^2 x^2 + 12)^{-1} \cdot (29 M_w^4 \pi^4 x^4 + 672 M_w^2 \pi^2 x^2 + 4608) + O(M_w^5) \tag{4.19}$$

This provides a ballistics criterion that is independent of the motor cross-section.

While a compact solution, Eq. (4.19) is a longer relation than its incompressible counterpart. If compressiblity effects are ignored the specific impulse becomes

$$(I_s)_{inc} = \frac{\pi^2 a_0}{8 g_0} M_w x \tag{4.20}$$

A comparison of the two terms over the length of a typical motor is presented in Figure 4.7. The first case presented is for the cold flow injection of air that has been used by Traineau for previous comparisons. A second, hot flow case is shown for a motor of similar size to cover a more realistic range of values for the specific impulse. Near the headwall, both the compressible and incompressible specific impulses follow the same linear relationship. Once the flow nears the midpoint of the chamber, the compressible expression diverges as the nonlinear terms in Eq. (4.19) begin to dominate. Equation (4.20) maintains its linearity for the entire length of the motor. The shape of the specific impulse axial distributions are the same for both cases. This is easily explained by the common dependence on a_0. In both the incompressible and compressible relationships, the speed of sound appears as a scaling parameter, multiplying both expressions equally. Therefore, for motors of similar injection speed and size, the speed of sound is the sole determining characteristic for increasing specific impulse performance.

It is also of interest to note that, if by scaling the length of the chamber by the sonic length, the specific impulse curve for a given value of the speed of sound will be the same for any variety of motor. For example, Figure 4.7 is generated using values based on Traineau's experimental case with a $L_s = 45.5$. If one is to use a lower value for injection, say $M_w = 0.0034$ which requires $L_s = 153.78$, creation of a similar plot will produce curves

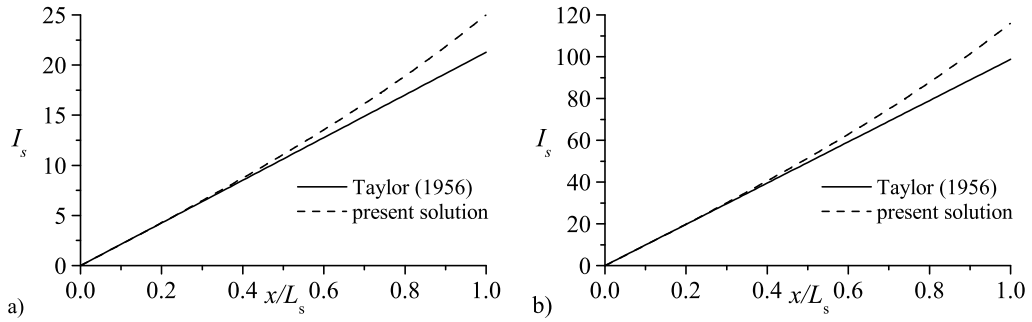


Figure 4.7: The specific impulse for a) $a_0 = 323$ m/s and b) $a_0 = 1500$ m/s.

that are identical to Figure 4.7 despite the fact that the injection Mach number is much smaller.

4.6.4 Characteristic Velocity

Another figure of merit is the characteristic velocity, c^*. The characteristic velocity is a comparative measure of propellant and combustion system performance. Because c^* is independent of the nozzle performance, it is ideal for evaluating nozzleless rocket performance. Sutton and Biblarz[37] define c^* as

$$c* = \frac{p_c A_t}{\dot{m}} \tag{4.21}$$

where p_c is the combustion chamber pressure, A_t is the throat area of the nozzle, and $\dot{m}$ is the mass flowrate through the motor. Because our analysis is not limited by a constant pressure throughout the combustion chamber, an average value of the chamber pressure will be calculated by integrating the pressure of the volume of the chamber and then dividing by the volume via

$$p_c = \frac{\int p dV}{V} = \frac{p_0}{L} \int_0^1 \int_0^L p \, dxdy \tag{4.22}$$

where L is the nondimensional length of the motor, normalized by the half-height. After evaluation, Eq. 4.22 becomes

$$p_c = p_0 \left[1 - M_w^2 \gamma \left(\frac{1}{4} + \frac{\pi^2}{24} L^2 + \frac{1}{32} M_w^2 - \frac{13\pi^2}{384} L^2 M_w^2 + \frac{\pi^4}{1920} L^4 M_w^2 \right) \right] \tag{4.23}$$

The result from Eq. (4.23) fully determines the right hand side of Eq. (4.21). After substitution one gets

$$c^* = \frac{12a_0\left[-1920/\gamma + 80M_w^2\left(6 + L^2\pi^2\right) + M_w^4\left(60 - 65L^2\pi^2 + L^4\pi^4\right)\right]}{5LM_w\left(12 + L^2M_w^2\pi^2\right)\left[-384 + 48L^2M_w^2\pi^2 + L^4M_w^4\pi^4\left(3\gamma - 2\right)\right]} \tag{4.24}$$

Figure 4.8 depicts the characteristic velocity for motors of varying length. The expression in Eq. (4.24) is singular at the origin. This is not surprising since the expression is very dependent on the length of the motor. For extremely small values of motor length, the denominator of Eq. (4.24) approaches zero and the result is an infinite characteristic velocity for a motor of zero length. When the length of the motor increases to the normal range of aspect ratios, the values of the characteristic velocity will quickly fall in line with the normal range of values expected for solid rocket motor operation.[37] The shape of the plot in Figure 4.8 suggests that while smaller chambers may be more efficient, not much efficiency is lost in longer motors since the curve approaches a fixed value as the length of the motor extends. However, with the longer motor one expects the increased thrust produced by the increased mass injection to result in a more powerful motor, offsetting the loss in characteristic velocity.

4.6.5 Thrust Coefficient

The final performance measure presented here is the thrust coefficient. Since the thrust coefficient is typically used as a measure of nozzle performance, its value in the nozzleless chamber application is limited, but it is included here for the sake of completeness. The relationship for the thrust coefficient is given by the following relation

$$C_f = \frac{F}{P_c A_t} \tag{4.25}$$

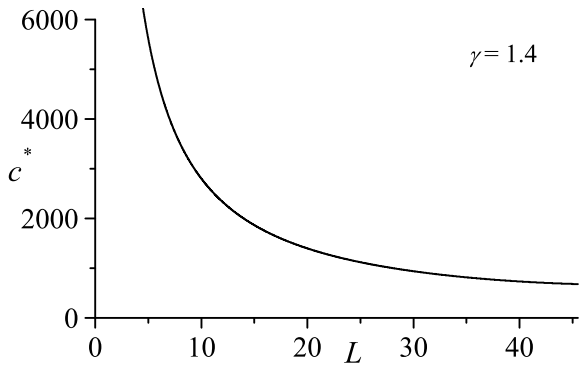


Figure 4.8: Evolution of the characteristic velocity.

The parameters of Eq. (4.25) have been completely determined previously in this section. Substitution of the known quantities produces

$$C_f = 5\pi^2 M_w^2 L^2 \left(29\pi^4 M_w^4 L^4 + 672\pi^2 M_w^2 L^2 + 4608\right) \times \frac{\left[(3\gamma - 2)\,\pi^4 M_w^4 L^4 + 48\pi^2 M_w^2 L^2 - 384\right]}{36864\left[-1920/\gamma + 80M_w^2\left(\pi^2 L^2 + 6\right) + M_w^4\left(\pi^4 L^4 - 65\pi^2 L^2 + 60\right)\right]} \tag{4.26}$$

The changes in the thrust coefficient for increasing motor length are shown in Figure 4.9. The curve starts at the origin which makes physical sense since motors of zero length should produce zero thrust and similarly zero thrust coefficient. As the motor length increases, so does the thrust coefficient. At the sonic length of the motor, $C_f = 0.5047$. While the exponential trend for increasing motor length is somewhat alarming, once the motor reaches the sonic length, the flow would choke and the thrust coefficient would be limited by its value at the sonic length of the nozzleless motor. This limiting effect prevents one from having to examine the case of an infinite thrust coefficient, which has no physical basis. For a typical rocket motor, values of the thrust coefficient vary from 0.8 to 1.9.[37] The difference between the observed values and those found in Figure 4.9 can be attributed to the absence of a nozzle in the present study. The expansion of the supersonic gases from the nozzle can greatly increase the thrust force, and as a result the thrust coefficient increases accordingly.

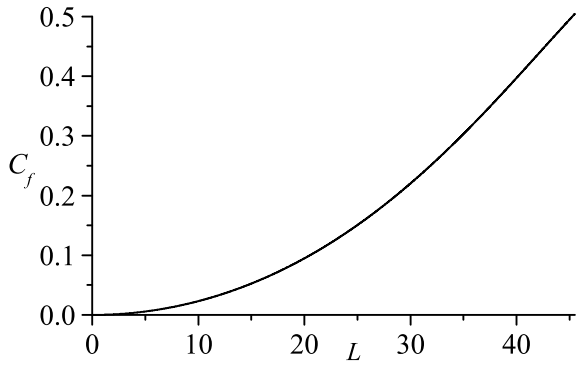


Figure 4.9: Thrust coefficient for increasing motor length.

The value of nozzleless performance characteristics on their own is limited. Currently nozzleless motors are not used in many applications, and as a result the demand for performance calculations for these motors is small. While the performance characteristics presented here are of varying degrees of usefulness to a nozzleless motor, all of the measures are good for comparison purposes with conventional, nozzled rocket motors. Many of the characteristics such as thrust, specific impulse, and thrust coefficient are heavily dependent on the nozzle configuration, but having a nozzleless analog can help determine exactly what portion of each characteristic is dependent on the nozzle design and what is reliant on the chamber design or combustion process. For the characteristics that are less dependent on the nozzle, these analytical expressions for the performance can be used to estimate the characteristics of the conventional motor and ensure that proper instrumentation is selected for testing.

Chapter 5

Conclusions

The Rayleigh-Janzen perturbation approach presented here yields a compact, closed form solution for compressible, inviscid flow in a two-dimensional geometry; when applied to a slab rocket flow field, results are found to be in good agreement with both computation and experiment. The closed form expressions for the variables of interest help to further the understanding of compressibility effects on the flow field of a solid rocket motor, where previously only one-dimensional, pseudo-two-dimensional, numerical, or experimental findings were available. When exact expressions are too cumbersome for analysis, approximate expressions have been provided. Practical relations and ballistics characteristics are also presented to aid in the design of both regular and nozzleless rockets.

The present study shows good agreement with both numerical and experimental studies. Variations from the numerical predictions in pressure can be accounted for by the neglect of viscosity. The underpredicted temperature field is not subject to viscosity but varies according to isentropic relationships. Velocity comparisons made throughout the chamber show good agreement with other experimental and numerical results. The compressible profiles capture the steepening behavior predicted by Balakrishnan *et al.*,[14] a feature that is now captured analytically.

To improve the predictive capability of this model, more effects should be included in the analysis. Incorporating viscous effects into the model is a natural extension for this

work. The normal injection boundary condition captures some traits of viscous behavior; however without accounting for viscosity throughout the flow, one expects the temperature distribution to underpredict experimental values. Allowing for viscosity, and the energy transfer associated with it, may bring the temperature in line with experimental prediction. The isentropic condition applied in this study is another restrictive condition that could be relaxed in favor of a more complete energy analysis. Instead of relying on the isentropic relations between pressure and the other thermodynamic variables, a more complete energy equation could be substituted to provide a more realistic model, particularly, an energy equation with a distributed heat source to simulate combustion effects.

The work presented in this thesis is valuable to the analysis of slab rocket motors and other rectangular channel flows. However, perhaps of greater value is that this study may serve as a proof of concept for studying internal, compressible flows in other geometries. The study could be extended to arbitrary geometries in both the two-dimensional and the axisymmetric case. It is also possible to extend the general analysis to other sorts of flows. One may use a similar approach to find a compressible analog for vortex motions such as those presented by Vyas *et al.*[38–40]

Bibliography

Bibliography

[1] White, F. M., *Viscous Fluid Flow*, McGraw Hill, 2nd ed., 1991.

[2] Berman, A. S., "Laminar Flow in Channels with Porous Walls," *Journal of Applied Physics*, Vol. 24, No. 9, 1953, pp. 1232–1235.

[3] Taylor, G. I., "Fluid Flow in Regions Bounded by Porous Surfaces," *Proceedings of the Royal Society, London, Series A*, Vol. 234, No. 1199, 1956, pp. 456–475.

[4] Culick, F. E. C., "Rotational Axisymmetric Mean Flow and Damping of Acoustic Waves in a Solid Propellant Rocket," *AIAA Journal*, Vol. 4, No. 8, 1966, pp. 1462–1464.

[5] Traineau, J.-C., Hervat, P., and Kuentamann, P., "Cold-Flow Simulation of a Two-Dimensional Nozzleless Solid Rocket Motor," *AIAA Joint Propulsion Conference*, No. 86-1447, Huntsville, Alabama, June 1986.

[6] Apte, S. and Yang, V., "Unsteady Flow Evolution in a Porous Chamber with Surface Mass Injection. Part I: Free oscillation," *AIAA Journal*, Vol. 39, No. 8, 2001, pp. 1577–1586.

[7] Najjar, F. M., Haselbacher, A., Ferry, J. P., Wasistho, B., Balachandar, S., and Moser, R., "Large-scale Multiphase Large-eddy Simulation of Flows in Solid-rocket Motors," *AIAA Computational Fluid Dynamics Conference*, No. 2003-3700, Orlando, FL, June 2003.

[8] Balakrishnan, G., Liñán, A., and Williams, F. A., "Compressible Effects in Thin Channels with Injection," *AIAA Journal*, Vol. 29, No. 12, 1991, pp. 2149–2154.

[9] Beddini, R. A. and Roberts, T. A., "Response of Propellant Combustion to a Turbulent Acoustic Boundary Layer," *Journal of Propulsion and Power*, Vol. 8, No. 2, 1992, pp. 290–296.

[10] Chu, W. W., Yang, V., and Majdalani, J., "Premixed Flame Response to Acoustic Waves in a Porous-walled Chamber with Surface Mass Injection," *Combustion and Flame*, Vol. 133, No. 6129, 2003, pp. 359–370.

[11] Zhou, C. and Majdalani, J., "Improved Mean Flow Solution for Slab Rocket Motors with Regressing Walls," *Journal of Propulsion and Power*, Vol. 18, No. 3, 2002, pp. 703–711.

[12] King, M. K., "Consideration of Two-dimensional Flow Effects on Nozzleless Rocket Performance," *Journal of Propulsion and Power*, Vol. 3, No. 3, 1987, pp. 194–195.

[13] Flandro, G. A., "Stability Prediction for Solid Propellant Rocket Motors with High-Speed Mean Flow," Final Technical AFRPL-TR-79-98, Air Force Rocket Propulsion Laboratory, Edwards AFB, CA, August 1980.

[14] Balakrishnan, G., Liñán, A., and Williams, F. A., "Rotational Inviscid Flow in Laterally Burning Solid Propellant Rocket Motors," *Journal of Propulsion and Power*, Vol. 8, No. 6, 1992, pp. 1167–1176.

[15] Gany, A. and Aharon, I., "Internal Ballistics Considerations of Nozzleless Rocket Motors," *Journal of Propulsion and Power*, Vol. 15, No. 6, 1999, pp. 866–873.

[16] Majdalani, J., "The Oscillatory Channel Flow with Arbitrary Wall Injection," *Journal of Applied Mathematics and Physics*, Vol. 52, No. 1, 2001, pp. 33–61.

[17] Liepmann, H. and Roshko, A., *Elements of Gasdynamics*, Dover Publications, Inc., 2001.

[18] Shapiro, A. H., *The Dynamics and Thermodynamics of Compressible Fluid Flow*, Vol. 1, The Ronald Press Company, 1953.

[19] Vuillot, F. and Avalon, G., "Acoustic Boundary Layers in Solid Propellant Rocket Motors Using Navier-Stokes Equations," *Journal of Propulsion and Power*, Vol. 7, No. 2, March-April 1991, pp. 231–239.

[20] Wasistho, B., Balachandar, R., and Moser, R. D., "Compressible Wall-Injeciton Flows in Laminar, Transitional, and Turbulent Regimes: Numerical Prediction," *Journal of Spacecraft and Rockets*, Vol. 41, No. 6, November-December 2004, pp. 915–924.

[21] Taylor, G. I., "The Conditions Necessary for Discontinuous Motion in Gases," *Proceedings of the Royal Society*, Vol. A84, 1910, pp. 371–377.

[22] von Mises, R., "On the Thickness of a Steady Shock Wave," *Journal of Aeronautical Sciences*, Vol. 17, 1950, pp. 551–555.

[23] Wilcox, D. C., *Elements of Fluid Mechanics*, DCW Industries, Inc., 2005.

[24] Ackeret, J., "Über Luftkräfte bei sehf grossen Geschwindigkeiten insbesondere bei ebenen Strömungen," *Helvetica Physica Acta*, Vol. 1, 1928, pp. 301–322.

[25] von Mises, R., *Mathematical Theory of Compressible Flow*, Vol. 3 of *Applied Mathematics and Mechanics*, Academic Press Inc., New York, 1958.

[26] Tsien, H.-S., "Two-Dimensional Subsonic Flow of Compressible Fluids," *Journal of the Aeronautical Sciences*, Vol. 6, No. 10, August 1939, pp. 399–407.

[27] von Kármán, T., "Compressiblity Effects in Aerodynamics," *Journal of the Aeronautical Sciences*, Vol. 8, No. 9, July 1941, pp. 337–356.

[28] Cohen, M. J., "High-Lift Airfoil Design from the Hodograph," *Journal of Aircraft*, Vol. 21, No. 10, 1984, pp. 760–766.

[29] Kaplan, C., "The Flow of a Compressible Fluid Past a Curved Surface," Tech. Rep. 768, NACA, 1943.

[30] Kaplan, C., "The Flow of a Compressible Fluid Past a Circular Arc Profile," Tech. Rep. 994, NACA, 1944.

[31] Kaplan, C., "Effect of Compressibility at High Subsonic Velocities on the Lifting Force Acting on an Elliptic Cylinder," Tech. Rep. 834, NACA, 1946.

[32] Janzen, O., "Beitrag Zu Einer Theorie Der Stationaren Stromung Kompressibler Flussigkeiten," *Phys. Zeitschr.*, Vol. 14, 1913, pp. 639–643.

[33] Rayleigh, L., "On the Flow of a Compressible Fluid Past an Obstacle," *Phil. Mag.*, Vol. 32, 1916, pp. 1.

[34] Majdalani, J., "The Compressible Taylor-Culick Flow," *AIAA Joint Propulsion Conference*, No. 2005-3542, Tuscon, AZ, 2005.

[35] Moore, D. and Pullin, D. I., "On Steady Compressible Flows with Compact Vorticity; The Compressible Hill's Spherical Vortex," *Journal of Fluid Mechanics*, Vol. 374, 1998, pp. 285–303.

[36] Meiron, D. I., Moore, D., and Pullin, D., "On Steady Compressible Flows with Compact Vorticity; The Compressible Stuart Vortex," *Journal of Fluid Mechanics*, Vol. 409, 2000, pp. 29–49.

[37] Sutton, G. P. and Biblarz, O., *Rocket Propulsion Elements*, John Wiley & Sons, Inc., 7th ed., 2001.

[38] Vyas, A. B., Majdalani, J., and Chiaverini, M. J., "The Bidirectional Vortex. Part 1: An Exact Inviscid Solution," *AIAA Joint Propulsion Conference*, No. 2003-5052, Huntsville, Alabama, July 2003.

[39] Vyas, A. B., Majdalani, J., and Chiaverini, M. J., "The Bidirectional Vortex. Part 2: Viscous Core Corrections," *AIAA Joint Propulsion Conference*, No. 2003-5052, Huntsville, Alabama, July 2003.

[40] Vyas, A. B., Majdalani, J., and Chiaverini, M. J., "The Bidirectional Vortex. Part 3: Multiple Solutions," *AIAA Joint Propulsion Conference*, No. 2003-5052, Huntsville, Alabama, July 2003.

Appendix

Appendix

Lower Order Critical Length Calculations

It is possible to determine the critical length of the motor to increasing degrees of accuracy by comparing results with fewer terms to results with all of the terms included. For a simple, rough approximation of the choke length, only the leading order terms are retained to give the expression

$$M_w \frac{\pi x}{2} = \sqrt{1 - M_w^2 \frac{(\gamma - 1)}{8} \pi^2 x^2} \tag{5.1}$$

Squaring both sides and collecting terms

$$\frac{\pi^2 M_w^2}{8} (\gamma + 1) x^2 = 1 \tag{5.2}$$

Finally, solving for x and keeping only the positive root gives the the expression for the leading order critical length

$$x_s = \frac{2\sqrt{2}}{M_w \pi \sqrt{\gamma + 1}} \tag{5.3}$$

Only the positive root for the choke length makes physical sense for determining the sonic length.

To illustrate how expensive the increase in accuracy is in terms of equation complexity, we retain the second order velocity terms to yield

$$M_w \frac{\pi x}{2} - M_w^3 \frac{\pi x}{96} \left(18 - 2\pi x^2\right) = \sqrt{1 - M_w^2 \left(\frac{(\gamma - 1)}{8} \pi^2 x^2 \right)} \tag{5.4}$$

A similar procedure is used, squaring both sides of Eq. (5.4). With the addition of the second order velocity, the solution becomes more complex.

$$\frac{M_w^6\pi^6}{2304}x^6 + \frac{M_w^4\pi^4}{384}(8-3M_w^2)x^4 + \frac{M_w^2\pi^2}{256}\left[32\left(\gamma+1\right) - 48M_w^2 + 9M_w^4\right]x^2 - 1 = 0 \tag{5.5}$$

The complexity of the equation for the sonic length goes up from a simple quadratic to a cubic equation. Solving Eq. (5.5) and selecting the real, positive root gives the following solution

$$x_s^{(1)} = \frac{1}{\pi M_w}\sqrt{\frac{9M_w^4 + 6M_w^2(\beta^{\frac{1}{3}} - 8) + \beta^{\frac{2}{3}} - 16\beta^{\frac{1}{3}} - 96\gamma + 160}{\beta^{\frac{1}{3}}}} \tag{5.6}$$

where β is

$$\beta = 32\left[4(18\gamma-5) + 9M_w^2(1-3\gamma) + 6\sqrt{2(9M_w^2(-4\gamma^2-3\gamma+5) + 2(6\gamma^3+6\gamma^2+30\gamma-25)}\right] \tag{5.7}$$

It is interesting to note that while Eq. (5.6) is dependent on the Mach number, it is only weakly so. An approximate expression for the choke length, neglecting terms higher than $O(M_w^2)$, can be written as

$$x_{sa}^{(1)} = \frac{1}{\pi M_w}\sqrt{\frac{\beta_a^{\frac{2}{3}} - 16\beta_a^{\frac{1}{3}} + 160 - 96\gamma}{\beta_a^{\frac{1}{3}}}} \tag{5.8}$$

where β_a is equal to

$$\beta_a = 128\left(18\gamma - 5 + 3\sqrt{6\gamma^3+6\gamma^2+30\gamma-25}\right) \tag{5.9}$$

The more compact, approximate expression for the choke length is accurate to three decimal places when compared to the full expression, for the range of injection Mach numbers common to slab rocket motor applications.

Vita

Brian Maicke was born in Waukeegan, IL on July 13, 1977. He attended Marquette University where he was a three time varsity letter winner as a member of the wrestling team. In the spring of 1999, he received a Bachelors of Science degree in Mechanical Engineering. After working in industry for five years, he began graduate studies at the University of Tennessee Space Institute in January of 2004. Brian studied Fluid Mechanics under the direction of Dr. Majdalani and will be graduating with a Master of Science degree in Aerospace Engineering in December of 2006. Brian plans to continue his studies at the University of Tennessee Space Institute to pursue his doctoral degree.